

# A 31 GHz Survey of Low-Frequency Selected Radio Sources

B.S. Mason<sup>1</sup>, L. Weintraub<sup>2</sup>, J. Sievers<sup>3</sup>, J.R. Bond<sup>3</sup>, S.T. Myers<sup>4</sup>, T.J. Pearson<sup>2</sup>, A.C.S. Readhead<sup>2</sup>, M. C. Shepherd<sup>2</sup>

## ABSTRACT

The Robert C. Byrd Green Bank Telescope (GBT) and Owens Valley Radio Observatory (OVRO) 40-meter radio telescopes have been used to conduct a survey of 3165 known extragalactic radio sources over  $143 \text{ deg}^2$  of the sky. Target sources were selected from the NRAO VLA Sky Survey in microwave background anisotropy fields observed by the Cosmic Background Imager (CBI). As a result of the GBT+OVRO survey measurements are made, or limits set upon, the 31 GHz flux densities of 3165 NVSS sources; the resulting 31 GHz catalogs are presented in full online. A Maximum-Likelihood analysis of these data yields an unbiased estimate of the distribution of the 1.4 to 31 GHz spectral indices of these millijansky radio sources, with typical values  $\alpha = -1.0$  (where  $S_\nu \propto \nu^\alpha$ ); 9% of sources have  $\alpha > -0.5$  and 1% have  $\alpha > 0$ . From these results and low frequency source counts we present an estimate of the 31 GHz source counts,  $N(> S_{31}) = (16.7 \pm 0.4) \text{ deg}^{-2} (S_{31}/1 \text{ mJy})^{-0.80 \pm 0.01}$  ( $0.5 \text{ mJy} < S_{31} < 10 \text{ mJy}$ ). Using the same distribution of  $\alpha_{1.4-31}$  and the CBI visibility dataset as inputs to a suite of Monte-Carlo simulations which run through the full CBI power spectrum pipeline, we assess the contribution of unresolved point sources to the CBI power spectrum. Unresolved point sources typically contribute less than 1/6 of the observed excess 31 GHz power at  $\ell > 2000$ , and even extreme instances of source populations give rise to less than half of the excess power, ruling out standard mJy-level radio AGN as a possible origin for this signal.

## 1. Introduction

Accurate measurements of cosmic microwave background (CMB) anisotropies on scales smaller than the sound horizon at last scattering are necessary to form a complete understanding of the initial power spectrum of cosmic inhomogeneities. Secondary anisotropies— chiefly reionization and Sunyaev-Zeldovitch (SZ) distortions from large scale structures— also leave imprints on these

---

<sup>1</sup>National Radio Astronomy Observatory, 520 Edgemont Road, Charlottesville, VA 22903

<sup>2</sup>Owens Valley Radio Observatory, California Institute of Technology, Pasadena, CA

<sup>3</sup>Canadian Institute for Theoretical Astrophysics, University of Toronto, ON M5S 3H8, Canada

<sup>4</sup>National Radio Astronomy Observatory, Socorro, NM 87801

scales which have clues to the subsequent evolution of structures from very simple, linear initial conditions to the wealth of nonlinear structures seen in the nearby universe. Photon diffusive damping occurring near last scattering has the effect of strongly suppressing small-scale intrinsic CMB anisotropies, however, so precise measurements on these scales are difficult. The primary limitation on the accuracy of current centimeter-wavelength observations on these scales is our knowledge of the variance contributed by faint, discrete radio sources.

In the particular case of the Cosmic Background Imager (Readhead et al. 2004, CBI) residual discrete sources contribute a variance of  $\sim 100 \mu\text{K}^2$  to the  $\ell > 2000$  signal<sup>1</sup>. This statistical contribution is subtracted from the CBI data, but is only known to  $\sim 50 \mu\text{K}^2$  and contributes a substantial uncertainty to the CBI “excess” measurement at high- $\ell$  of  $346 \pm 113 \mu\text{K}^2$ . Here the  $113 \mu\text{K}^2$  error bar indicates thermal noise only. In the CBI power spectrum analysis all *known* radio sources are removed by “projecting” them out of the analysis<sup>2</sup>. The 1.4 GHz NRAO VLA Sky Survey (NVSS Condon et al. 1998) covers the entirety of the CBI CMB fields, and we remove all radio sources down to 3.4 mJy, near its nominal detection limit of 2.4 mJy. The statistical correction to the power spectrum comes from the sources below  $S_{1.4} = 3.4 \text{ mJy}$ , *and thus it is fundamentally a low-frequency selected population*. We must, however, know the variance that this population contributes to the 31 GHz sky. Previous to the work we report here the uncertainty in the correction is dominated by the poorly constrained extrapolation of 1.4 GHz flux densities to 31 GHz.

If sources below some cutoff flux density  $S_{max}$  are included in the statistical correction, it can be expressed as (Myers et al. 2003)

$$C_{src} = \int_0^{S_{max}} dS S^2 \frac{dN}{dS} \quad (1)$$

In our case, however, the sources are selected for inclusion at a different, lower frequency, (*i.e.*, they are in effect the sources in our fields that are not detected reliably in the NVSS, hence are not projected out). Then, assuming that the spectral properties of the sources are constant over the range of relevant flux densities, Eq. 1 becomes

$$C_{src} = \left\langle \left( \frac{s_{31}}{S_{1.4}} \right)^2 \right\rangle \int_0^{S_{max,1.4}} dS_{1.4} S_{1.4}^2 \frac{dN}{dS_{1.4}} \quad (2)$$

The low-frequency source counts  $\frac{dN}{dS}$  are well-known. To accurately correct 31 GHz CMB measurements for point source contamination we need to determine the mean value of  $\left( \frac{s_{31}}{s_{1.4}} \right)^2$  and its distribution. In these units the small-scale power seen by the CBI, if caused exclusively by

---

<sup>1</sup> $\ell > 2000$  corresponds to  $\sqrt{u^2 + v^2} > 600$ , or angular scales smaller than 5 arcminutes.

<sup>2</sup>“Source projection” is a procedure equivalent to allowing an arbitrary variance to a linear combination of the data corresponding to the point source. This procedure is performed in fourier space; the analog in the image domain would be deleting a contaminated pixel.

point source contamination, corresponds to  $C_{res} = 0.23 \text{ Jy}^2 \text{ sr}^{-1}$ . For the shallow source counts  $[N(> S) \propto S^{-0.7}]$  observed at mJy levels the sources immediately below the projection threshold dominate the sky variance and our surveys preferentially targets this population. At 31 GHz the sky variance can be strongly influenced by the abundance of comparatively rare flat or inverted spectrum sources, and to place useful constraints on these sources a large sample is needed.

In this paper we present a detailed characterization of the impact of the discrete source foreground on arcminute-scale 31 GHz anisotropy measurements based upon two observational campaigns. The first campaign was carried out with the Owens Valley Radio Observatory (OVRO) 40-meter telescope at 31 GHz from September of 2000 through December of 2002. The second was carried out with the Robert C. Byrd Green Bank Telescope (GBT) from February to May of 2006. This work was undertaken with the specific aim of improving the accuracy of CBI microwave background anisotropy measurements. A companion paper (Sievers et al. in prep.) presents the 5-year CBI total intensity power spectrum incorporating the results of the point source measurements discussed here.

The structure of this paper is as follows. In § 2 we describe the instrumentation used in both surveys. § 3 describes the source lists and sample selection. § 4 describes the OVRO 40-m and GBT observations and data reduction and presents catalogs of the observations. § 5 presents a determination of the 1.4 to 31 GHz spectral index of NVSS sources and determines the implications of these measurements for 30 GHz CMB observations, for the case of the CBI in particular; here we also present a determination of the 31 GHz source counts. Finally § 6 reviews our main conclusions.

## 2. Instrumentation

### 2.1. OVRO 40-meter and 31 GHz Receiver

In 1999 the OVRO 40-meter telescope was outfitted with a Dicke-switching, dual horn receiver operating in four 2 GHz bands between 26 and 34 GHz. The Dicke switch alternates between the two horns at a rate of 125 Hz, sampling two beams separated by  $7'.8$  in cross-elevation on the sky. Each beam has a FWHM of  $1'.36$  at 31 GHz; this is somewhat larger than what would be expected for a 40-meter dish since only the central 30 meters are illuminated. The measured receiver temperatures in each of the four bands are between 38 K (in the 27 GHz band) and 23 K (in the 31 GHz band). The higher receiver temperature in the lowest frequency band is due to losses in the Dicke switch. The statistics of (noise) samples taken against both ambient temperature and 77 K beam-filling loads are consistent with the receiver temperatures we have measured. Including 13 K per airmass due to the atmosphere, 2.7 K from the CMB, and a fixed ground contribution of 10 K, the system temperatures at zenith in the four bands range between 50 K and 60 K. Calibration is facilitated by two broad-band noise diodes; cross-guide couplers before the Dicke switch allow for the insertion of signals from these devices.

The telescope is an alt-azimuth instrument consisting of a paraboloidal dish reflector, primary focus feed and supports, mounted on an alidade and base pedestal. Our observing frequency of 31 GHz is beyond the design specification of the 40-meter telescope, resulting in aperture efficiencies of only 15%. The gain of the 40-m changes as a function of zenith-angle (ZA) due to gravitational deformations in the dish structure. These variations were characterized by long tracks on bright calibrators and the resulting gain corrections are applied offline in the data reduction. The focus position also varies with zenith angle. Attempts to characterize this dependence were difficult until it was found that the residuals to the ZA fit are well correlated with the angle of the sun from the optical axis. This additional optical deformation of the telescope is not surprising given the challenging frequency regime in which it is being operated. We find good repeatability of the zenith angle/sun-angle focus curves. The focus curves are applied in real time, and checked periodically for consistency. The peak sensitivity that the 40-meter achieves is 12 mJy RMS in one minute at 40 degrees elevation in the 29 and 31 GHz bands. The 27 and 33 GHz bands had substantially lower peak sensitivities of 31 and 22 mJy RMS, respectively.

## 2.2. GBT, 31 GHz Receiver and Continuum Backend

Broadband measurements of the radio-frequency continuum are affected by systematic effects such as gain fluctuations and variation in the emissivity of the atmosphere. The receiver built for the OVRO 40-m employed a Dicke switch to this end, enabling two feeds to be sampled rapidly in series. For the GBT receiver, we chose an electronic beamswitching arrangement employing 180° hybrids similar to the WMAP radiometers (Jarosik et al. 2003). This choice permits a wider bandwidth to be covered, avoids expensive and difficult to procure Dicke switches, and permits signals from both feeds to be simultaneously measured at all times. The initial design for a continuum receiver covering the 26 to 40 GHz band (Padin 2001) was updated to include spectroscopic capabilities and built in Green Bank, with first light in 2005. A block diagram of the receiver as constructed is shown in Figure 1, excluding the spectral line section which supports both traditional autocorrelation spectroscopy as well as broadband cross-correlation measurements. The continuum section completely bypasses the frequency conversions associated with the spectral line section, providing 16 RF detectors (one for each of four frequency bands times two feeds times both circular polarizations) and associated low-noise circuitry. Receiver temperatures range from 20 K to 40 K across the band, resulting in  $T_{sys}$  values on-sky of 35 K to 65 K. Broadband noise diodes are coupled in to the signal path prior to the first hybrid tee and permit monitoring the total gain of the system for calibration purposes.

The Caltech Continuum Backend (CCB) is a digital backend which controls the GBT Ka-band receiver and synchronously reads out and demodulates the beamswitched signal. Up to 16 RF detector outputs are simultaneously measured, corresponding to the 2 feeds x 2 polarizations x 4 frequency channels that the 26-40 GHz receiver provides. The CCB uses four “daughter cards”, each with a Xilinx XC3S400 FPGA chip which reads out four 10 MHz, 14-bit ADCs; a master card

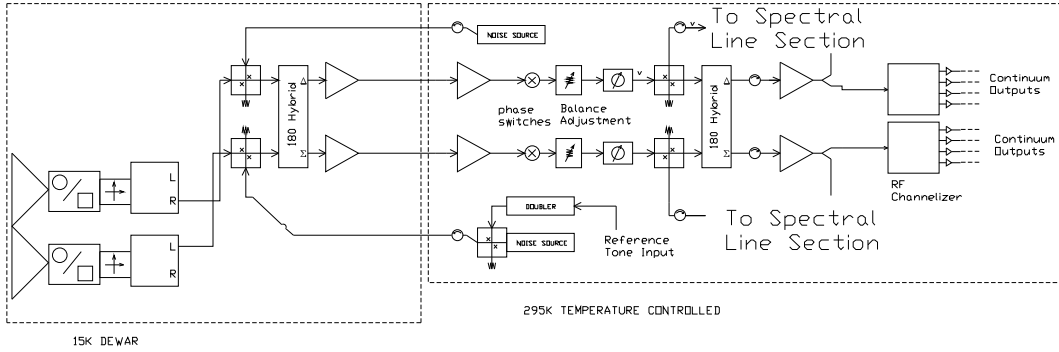


Fig. 1.— Block diagram of the GBT Ka-band receiver. This diagram shows half of the continuum section, with the other feed/polarization combination covered by a duplicate radiometer.

(also with an XC3S400) generates the receiver control signals, controls and reads out the daughter cards, and sends the data on to a host linux computer. The CCB is enclosed in an RFI tight box which shields other instrumentation (the CCB is mounted in the GBT receiver room), and also protects the sensitive analog circuitry in the CCB from externally generated RFI. The CCB itself contributes negligibly ( $< 0.1\%$ ) to the noise in a differenced power measurement with the receiver. Lab tests conducted with the CCB connected to the receiver show that the noise obtained is roughly 15 to 30% above the theoretical noise minimum given by the radiometer equation. While the CCB supports beam switching at up to 20 kHz, the phase switch drive circuit in the receiver responds more slowly and  $30\mu\text{sec}$  of blanking is required after each phase switch transition. For observations the receiver was operated with a 4 kHz beam switch rate in order to avoid excessive lost of time to blanking after phase switch transitions. The CCB was constructed by NRAO and the California Institute of Technology, with funding provided to Caltech through the NRAO University Instrumentation Program. The Ka-band receiver and CCB are available as facility instruments on the GBT<sup>3</sup>

<sup>3</sup>The receiver has subsequently been modified to support a full-receiver-band analog spectrometer (Harris et al. 2007). This eliminates half of the 16 CCB channels and, due to a change to linearly polarized feeds, complicates calibration, but improves radiometric balance and the performance of the high and low frequency channels.

The Robert C. Byrd Green Bank Telescope (GBT) is a 100-meter off-axis Gregorian telescope located in Green Bank, West Virginia (Jewell & Prestage 2004). The primary reflector comprises 2004 aluminum panels; the panel corners are mounted on actuators used to maintain a parabolic form. During observations the actuators’ locations are set based on the telescope elevation at the beginning of each scan (typically 70 sec of observing) using a look-up table. This look-up table was determined from Out-of-Focus Holography measurements of bright sources at a wide range of elevations (Nikolic et al. 2006). The OOF corrections remove deformations of the dish surface on scales of  $\sim 10$  m or larger result in an overall telescope gain which does not vary significantly above 20 degrees elevation. At 31 GHz the GBT aperture efficiency is 50%. The 2-dimensional RMS referenced pointing accuracy is  $4''$  on timescales of half an hour to an hour. Corrections to the focus tracking model on the same timescale are typically a few millimeters. With the 31 GHz receiver and continuum backend, we attain thermal noise limited performance ( $\sim 0.150$  mJy RMS in one minute) a small fraction of the time, when the atmosphere is very dry and stable. More typically the thermal noise RMS in a 60 second double-differenced observation (essentially identical to that described in § 4.1) is  $0.4 - 0.5$  mJy (RMS) in the center of the receiver band, and 1-3 mJy RMS in the outer frequency bands.

### 3. Source Lists and Sample Selection

Including a  $45'$  buffer zone, the CBI total intensity mosaic fields of Readhead et al. (2004) covered  $98 \text{ deg}^2$  of sky. The OVRO 40m survey targeted all  $S_{1.4} > 6 \text{ mJy}$  sources in this region. The CBI polarization observations (Sievers et al. 2007) covered  $115 \text{ deg}^2$  in all, also including a  $45'$  buffer zone; accounting for the overlap between these two datasets the total sky coverage is  $143 \text{ deg}^2$ . The GBT survey targeted  $S_{1.4} > 3.4 \text{ mJy}$  (the NVSS 99% completeness limit) sources in this total region, although full coverage was not achieved. Source selection proceeded from areas of sky with the lowest CBI map noise. Sources detected at  $3\sigma$  or greater in the OVRO survey as a rule were avoided in the GBT survey.

Sources in this region were observed from September 1999 through December 2001 with the OVRO 40-meter telescope in support of ongoing CBI observations. The 40-m observations preferentially targetted sources in the original (Pearson et al. 2003; Readhead et al. 2004) CBI total intensity fields; in all, 2,315 sources were observed by the 40-m. With the typical RMS sensitivity of the OVRO survey ( $2.5 \text{ mJy}$  – see § 4.1), this resulted in 180 detections at  $4\sigma$  or greater significance (363 at  $3\sigma$  or greater).

Our aim with the GBT survey was to measure *all* of the NVSS sources in the CBI fields with a sensitivity comparable to the RMS noise in the CBI maps. The 363 sources previously detected<sup>4</sup> at

---

<sup>4</sup>Due to a software bug, GBT observations of sources between  $+01^\circ$  and  $-01^\circ$  were observed without regard for the OVRO 40m measurements, *i.e.* observations in this range were not pre-censored by the measured OVRO flux value.

$3\sigma$  or greater in the OVRO 40m survey were not observed by the GBT, leaving 5,636 sources. Useful GBT data were collected on 1,490 of these (§ 4.3). Faint NVSS sources, and sources in areas where the CBI maps are most sensitive, were preferentially targeted. 640 of the OVRO observations were superseded by more sensitive GBT observations, leaving 1675 unique observations in the OVRO dataset. In all useful data were obtained on 3165 NVSS sources. The distribution of 1.4 GHz flux densities of the sources measured is shown in Figure 2.

## 4. Observations

### 4.1. OVRO Observations

All NVSS sources brighter than 6 mJy were observed to a typical RMS sensitivity of 2.4 mJy, requiring 30–5 minute observations on average. 5-minute observations of NVSS-selected sources were interleaved with daily measurements of 3C286, 3C147, 3C279, and other bright sources for calibration and to monitor the system’s performance. In between calibrator observations, the system gain was monitored with the noise diodes internal to the receiver. Every 40 minutes, a calibrator source within  $\sim 15^\circ$  of the field being observed was measured to determine the telescope pointing offset. For each flux density measurement, the online system reports an estimate of the measurement error from the variance in the 1-second samples within the integration period. During the course of all observations weather data are collected and recorded for later correlation with the astronomical datastream. The basic measurement consists of four beamswitched integration periods wherein the source of interest is alternately placed in the two beams of the telescope in an A/B/B/A pattern. This symmetric double-differencing scheme is effective at cancelling constant and gradient terms in atmospheric emission (Readhead et al. 1989).

The original CBI and OVRO 31 GHz flux density scale is based on the Mason et al. (1999) value for  $S_{3C286,32\text{ GHz}} = 2.02 \pm 0.07$  Jy, and spectral index  $\alpha = -0.8$  corresponding to a brightness temperature of for Jupiter of  $T_J = 152 \pm 5$  K. For the current work we adopt the WMAP 5-year (Hill et al. submitted) value  $T_J = 146.6 \pm 0.75$  K, slightly lower than the  $147.3 \pm 1.8$  K assumed in Readhead et al. (2004), but consistent within  $1\sigma$ . We extrapolate this calibration across the 40m bandpass using  $\alpha = -0.827$  (Leitch et al. 2000). Observations of 3C286, 3C48, and 3C147 from Sep 1999 through May of 2000 showed uncorrelated RMS variations in flux density of  $\sim 4\%$ . These variations were different for each source at high and low zenith angles, and uncorrelated with the calibration diode equivalent flux densities, all of which we take as indicative that there are residual gain and focus variations in the instrument calibration at this level. Together with the 3% uncertainty in the absolute flux density of 3C286, this gives a 5% calibration uncertainty for the OVRO 40-m.

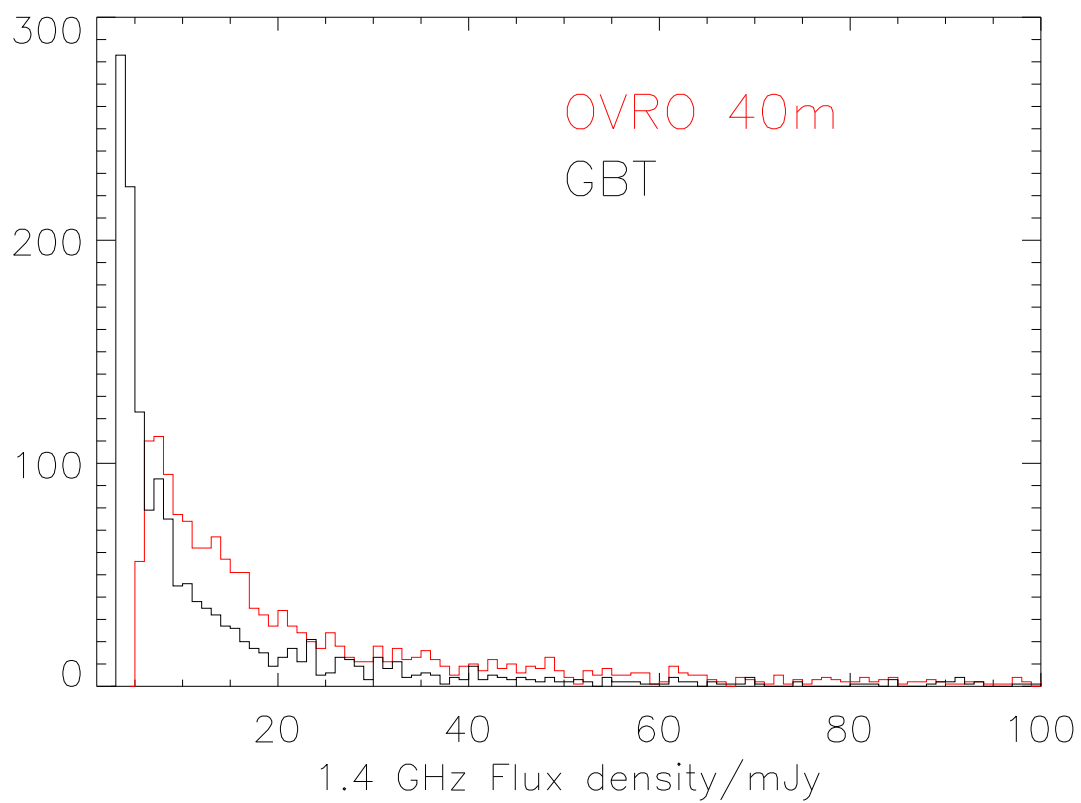


Fig. 2.— NVSS flux densities for sources measured in the GBT and OVRO 40-m surveys.



## 4.2. OVRO Data Reduction

OVRO data were reduced as follows. Observations of the noise diodes several times per hour are first used to remove electronic gain fluctuations and scale the data to antenna temperature. Corrections for the telescope gain as a function of elevation, determined from long tracks on bright calibrators, are applied, as is a correction to account for atmospheric opacity as a function of elevation. Observing campaigns several years in duration (Leitch et al. 2000) have determined that a single value of the atmospheric opacity per airmass,  $\tau = 0.045$ , suffices during the useful 31 GHz weather at the Owens Valley. We adopt this value.

Time-variable weather conditions determine the sensitivity of OVRO 40-m flux density measurements. Typically sources are observed in rotation, with 5 1-minute observations of each source. The typical timescale on which changes in the weather affect the 40-m photometric sensitivity is an hour, which sets the timescale on which we wish to estimate the measurement noise. During this period of time  $\sim 10$  separate sources with different mean flux densities will be measured. Typical sources in the OVRO sample are expected to have 31 GHz flux densities of 1 – 2 mJy, small in comparison to the 10 – 15 mJy noise level achieved on a per-observation basis. To determine the measurement noise for a single observation, we wish to compute the characteristic scatter of similar observations nearby in time with no contribution due to the scatter in the source flux densities themselves, the main concern being the power-law tail of the source flux density distribution which results in rare objects comparable to or greater than the per-observation noise level which could bias a scatter-based noise estimate. We chose to determine the noise level of each observation by computing the median absolute deviation of similar observations within a one hour buffer centered on the observation under consideration. The median absolute deviation (MedAD) of some data  $x_i$  is defined as

$$\text{MedAD}(x_i) = \text{Median}(|x_i - \text{Median}(x_i)|) \quad (3)$$

and is known to be a measure of the dominant noise scale of a distribution which is extremely resistant to the presence and magnitude of outliers (Hoaglin et al. 1983). For a Gaussian distribution of width  $\sigma_g$ , the  $\text{MedAD} = 0.6745\sigma_g$ . We use this relation to rescale the MedAD into an effective Gaussian  $\sigma$  value for each observation. An independent noise estimate is provided by the scatter of 1-second integrations *within* each measurement. The internal noises give results comparable to, but generally 15%-30% lower than, the scatter between observations. This is consistent with the expectation that except in the very best observing conditions, low-level photometric instabilities (*e.g.* a slow variation in the gradient of the sky emission) on timescales longer than that of an individual source observation contribute to the measurement noise. Straightforward simulations show that to within a few percent this approach yields an unbiased estimate of the RMS of a Gaussian noise distribution in the presence of power-law source populations with typical signal-to-noise ratios of 0.1 to 0.2.

Over the course of the observing campaign individual sources in our sample were observed between a few and about 100 times, most commonly about thirty times. All observations of a given

source are combined to form a weighted mean and an uncertainty on this mean is computed by propagation of the error bars of each measurement. The reduced  $\chi^2$  of the data about this average is also computed; these values are shown in Figure 3. Throughout the pipeline all 4 frequency channels are treated independently. For reference the expected distribution of  $\chi^2_\nu$  for 30 DOF is shown. There is a fairly broad distribution of final sensitivities, owing largely to the range of total integration times per source, but also to the range of photometric conditions. For our final source catalog (§ 4.7) we adopt a  $4\sigma$  detection threshold; the probability of detecting a given source at this level, allowing for the distribution of noises in our dataset, is shown in Figure 4.

Data within 5 degrees of the moon or the moon were rejected, as were data for which the preceding successful pointing calibrator observations was not successful and did not occur within one hour. Since high winds can affect the telescope pointing, observations during which the wind was greater than 15 mph are discarded. Reducing the pointing requirement from an hour to a half-hour, and the wind limit from 15 to 7.5 mph (reducing the force of the wind on the telescope by roughly a factor of four ) did not significantly affect the measured flux densities of the OVRO-detected sources.

For each band, the mean flux density for each source is computed by averaging over the entire observing epoch, with each point inversely weighted by the estimated measurement variance. In practice the outer (27 and 33 GHz) bands have little sensitivity due to increased noise from the Dicke switch and degraded aperture efficiency (at high frequency). For our final results we use only the 30 – 32 GHz band, which we take to have a nominal center frequency of 31.0 GHz. This is the center of the CBI observing band and corresponds closely to the most sensitive channel of the GBT receiver, readily allowing direct comparisons.

### 4.3. GBT Observations

Test observations of the CCB and Ka-band receiver on the GBT were conducted in November and December of 2005, and January of 2006; these observations confirmed lab measurements of the system performance. The science observations ran from 02 February, 2006 through 07 May 2006. 3198 observations of 3040 NVSS sources were collected; after the data filtering described below, 1567 observations of 1490 sources remain in the final dataset.

For these observations we developed an “On-the-Fly Nod” variant of the double-differencing technique described in § 4.1 and Readhead et al. (1989). With this technique data are collected contiguously through the entire observation, including the slews between beams, and the recorded (10 Hz) antenna positions are later used with the target source coordinates to construct a template beamswitched signal which is fitted to the differenced data. This approach minimizes scan-start overheads and provides a conveniently continuous datastream for each source; it also allows for imperfect source acquisition and settling times to be accounted for carefully offline. An example observation of a bright sources is shown in Figure 5. A typical feature is the spike (really a dip

Fig. 3.—  $\chi^2_\nu$  distribution for OVRO 40m measurements, each individual  $\chi^2_\nu$  value being derived from the combination of all data in a given frequency band on a given source. Also shown is the theoretical reduced  $\chi^2$  distribution for 30 degrees of freedom, which is typical although the number of observations on a given source ranges from three to a hundred in some cases.

Fig. 4.— The probability that a given source is detected in the OVRO survey as a function of 31 GHz flux density. The 90% (dotted) and 95% (dash-dotted) completeness levels are shown for clarity. The GBT survey is essentially complete above 2.5 mJy.

in the source signal coming from the negative beam) arising from stiction in the telescope servo resulting in overshooting the source slightly when slewing in one direction. Since this overshoot is recorded by the antenna position encoders it is reflected in the template model and has minimal effect on our observations, particularly of our much weaker science sources. The on-source dwell time in each phase is 10 seconds; there is a 10-second slew between A and B phases. A 10 second settle was also allowed at the start of each scan in order to allow possible GBT feedarm vibrations (occasionally excited by the servo system at the start of a scan) to settle, but this was never seen to be an issue in our frequent bright-source calibration checks. The average slew-time between program sources was 20 seconds, for an average total elapsed time per source measurement of 90 seconds. During the nod measurement the detected RF power in each of 16 channels is recorded at 200 Hz by the CCB.

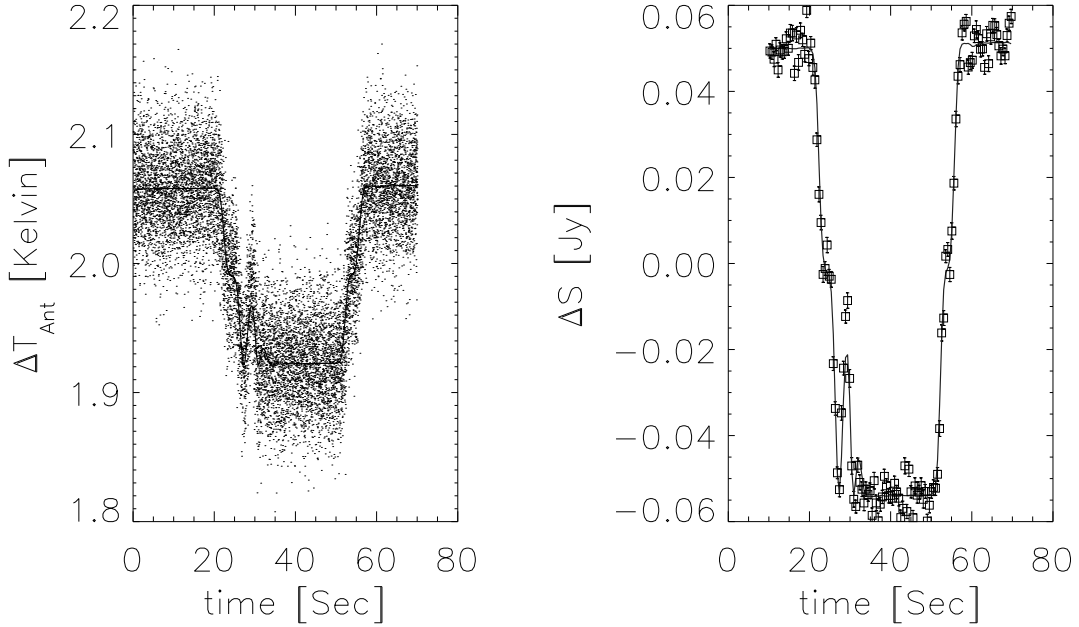


Fig. 5.— Measurement of steep spectrum source 085328 – 0341, channel J11, 31.25 GHz. The left hand plot shows the individual 5 millisecond beamswitched integration calibrated via the noise diode to antenna temperature. The right hand plot shows the individual beamswitched integrations averaged into 0.5 second measurements with error bars given by the internal scatter of each 0.5 second measurement and flux density calibrated via 3c286; here the initial 10 second settle period has been excised. The remaining data illustrates the symmetric A/B/B/A nod pattern in which the source was placed in the two beams of the receiver. The solid line in the right panel shows the template fit (Eq. 4).

During daylight the GBT pointing and focus was checked every half hour on a nearby bright

source ( $S_{31\text{ GHz}} > 500\text{ mJy}$ ); at night, this was relaxed to every 45 minutes. During each pointing and focus check a nod observation was also collected to monitor intraday stability of our measurements. To monitor interday repeatability of our calibration, we selected a steep-spectrum (NVSS/OVRO) source near each CBI field as well and measured it at least once per observing session.

#### 4.4. GBT Data Reduction

While the GBT observations are similar to the OVRO observations, several important differences lead to a slightly different approach to reducing the data. First, substantially less “data reduction” (averaging) is performed by the online data acquisition system, enabling preservation of more data for further diagnostics offline. Second, the typical signal-to-noise in a GBT observation is of order unity owing to the higher sensitivity of the telescope – see Figure 6. Finally the dataset is substantially smaller, less than a week in total in contrast to several years of OVRO observations. The overall approach is to record the timestream of the antenna positions and the 16 CCB channels in a single contiguous record for a symmetric Nod observation of a given source.

The CCB data are first averaged from 5 ms to 0.5 sec integrations  $d(t_i)$  and each integration is assigned an error estimate based on the scatter of the beamswitched 5 millisecond integrations within it. The 10 Hz recorded antenna positions are interpolated onto the same time sampling as the CCB data resulting in a time series of positions  $\vec{x}_j(t_i) \equiv \vec{x}_{j,i}$  for a given feed indexed by  $j = 1, 2$  for a given observation. The beam locations on the sky and measured GBT beam pattern  $B$  as a function of frequency are used to compute the expected beamswitched response of the receiver to a point source of flux density  $s_o$  at the location of the source of interest,  $\vec{x}_o$

$$d_i = s_o \times [B(|\vec{x}_{1,i} - \vec{x}_o|) - B(|\vec{x}_{2,i} - \vec{x}_o|)] + \langle d_i \rangle + \frac{dd_i}{dt} \quad (4)$$

where the difference in square brackets comes about due to the beam switching. The last two terms are mean (radiometric offset) and gradient terms allowed in the fit and which, due to the symmetry of the nod pattern, are approximately orthogonal to the source flux density parameter  $s_o$ . This template is fit directly to the beamswitched data – refer again to Figure 5 for an example. The  $\chi^2_\nu$  of the fit is good diagnostic of data quality; for sources weaker than 10 mJy,  $\chi^2_\nu$  is close to unity under good conditions, and as weather conditions degrade our simple model fails resulting in appreciable increase of the  $\chi^2_\nu$ . For sources brighter than  $\sim 10\text{ mJy}$   $\chi^2_\nu$  rarely approaches unity even under excellent observing conditions due to imperfections in the beam model and residual pointing errors. These observations require separate consideration in  $\chi^2_\nu$ -based filters.

This procedure is initially performed separately on each of the 16 CCB data channels. Using observations of 3C286 throughout the observing campaign a single mean calibration, referenced to the WMAP-5 Jupiter-temperature scale described in § 4.1, is determined for each channel. For the final processing this calibration is applied to the individual detector timestreams and all

timestreams for a given frequency are averaged in the time domain before performing the source flux density fit of Eq. 4. This ensures that noise fluctuations that are correlated between feeds or polarizations are correctly accounted for in the noise estimate that follows. Repeated observations of bright, steep-spectrum sources near our fields (also of fainter steep-spectrum sources) provide a check on the validity of our pointing filters. We find that the accuracy of our calibration for an individual source is 10% (RMS) at 31 GHz, dominated by uncertainties in the GBT pointing.

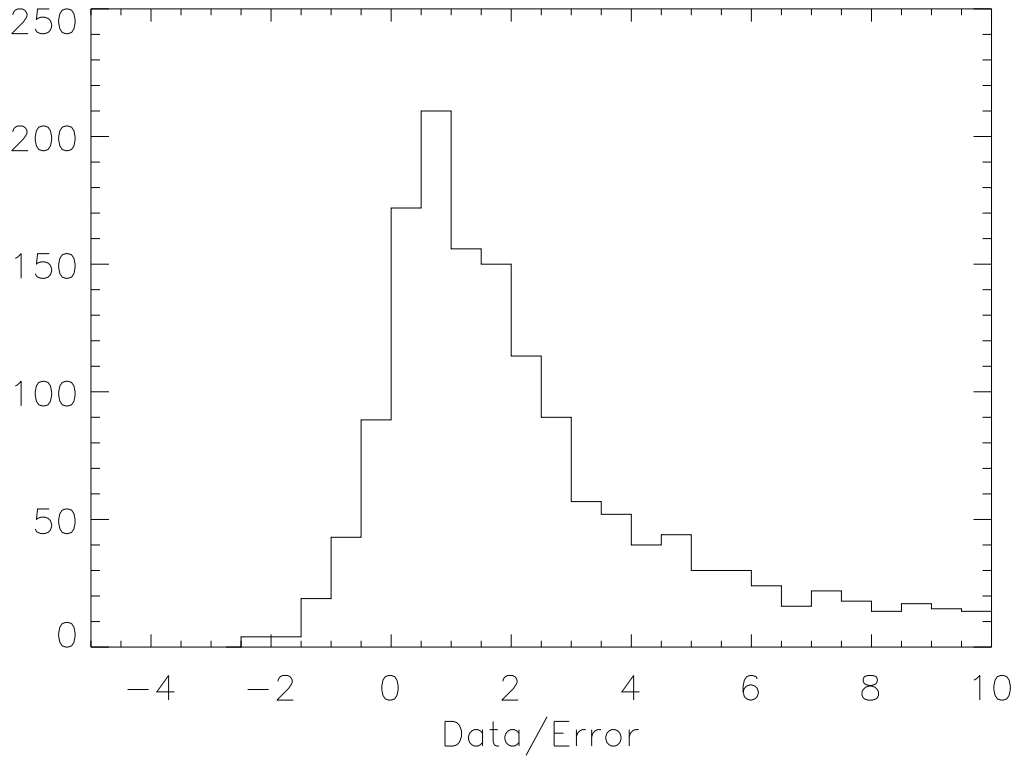


Fig. 6.— Histogram of GBT measurements divided by their individual noise estimates.

Since the signal to noise in a typical 70-second GBT observation is of order unity we cannot straightforwardly compute the noise in our data from the scatter of the measurements (*i.e.*, the fitted values of the source flux densities  $s_o$ ) themselves as we did for the OVRO measurements. We can, however, form alternate combinations of the individual segments of the symmetric Nod procedure to quantify the photometric stability of the measurement. If we designate the average value of integrations within individual segments of the nod by  $A_1, B_1, B_2, A_2$ , then  $\Delta A = A_1 - A_2$  is a source-signal-free combination measuring to the photometric fluctuation over 50 seconds, and  $\Delta B = B_1 - B_2$  is a source-signal-free combination measuring the photometric fluctuation over 10 seconds. From test observations of blank patches of sky under a wide range of conditions we find that the average (over some window of many observations) of the root-mean-squares of  $\Delta A$

and  $\Delta B$  gives an estimate of the RMS of the measured flux density values  $s_o$  accurate to within 10%. Note that since both  $A$  and  $B$  respond to time gradients of the beamswitched signal, whereas the fitted source flux density ( $s_o$  in Eq. 4) does not, we might expect to slightly overestimate the noise. To improve the robustness of this noise measure, in practice we compute the mean absolute deviation (MnAD) of  $\Delta A$  and  $\Delta B$  rather than the RMS and renormalize to a Gaussian equivalent ( $MnAD = \sqrt{2/\pi}\sigma_g$ ); we choose the somewhat less robust but lower variance MnAD over the MedAD used in § 4.2 because outliers are a lesser concern for the signal-free estimators  $\Delta A, \Delta B$  than in the flux density measurements themselves. For each measurement we compute these quantities in a one-hour buffer centered on the observation in question. With the appropriate normalization constants, derived in the white-noise limit, this gives a noise estimate

$$N(t_i) = \frac{\sqrt{\pi}}{8} [MnAD(\Delta A) + MnAD(\Delta B)] \quad (5)$$

(where the mean absolute deviations are computed from all observations within plus or minus a half hour of  $t_i$ ) close to the RMS that signal-free nod measurements would have under the same conditions. The data from the blank-field test observations are shown in Figure 7, normalized by the individual estimated measurement errors. The actual per-measurement noises varied by a factor of four. The dispersion in the noise-normalized data is  $\sigma = 0.91$ , acceptably close to the  $\sigma = 1.0$  which would result from perfectly measured Gaussian noise. As expected the noise is slightly overestimated due to the presence of radiometric gradients. In the NVSS-source survey the mean noise level in the data which pass the data filters described below is  $390 \mu\text{Jy}$ . The distribution is shown in Figure 8.

The main time-variable systematics that affect our data are departures from good photometric conditions caused by atmospheric clouds and water vapor and telescope pointing and focus. A series of filters excises compromised observations. To identify periods of poor photometry we compute the median  $\chi^2_\nu$  in sliding one-hour buffers – excluding measurements brighter than 10 mJy – and reject observations for which this value exceeds 1.4. To catch rare isolated glitches, individual observations with  $\chi^2_\nu > 1.4$  are also rejected *unless* the fitted flux density exceeded 10 mJy. In this case the observation is inspected manually (all are retained).

In the course of commissioning and operations the pointing and focus performance of the GBT has been extensively characterized, with results summarized by Condon (2003) and Balser et al. (2006). Under calm conditions (winds under 3.0 m/s) the observed RMS in the radial pointing offset is  $2.7''$ , corresponding to less than 5% loss of peak signal for the GBT’s  $24''$  (fwhm) beam at 31 GHz. When the windspeed is greater than a few meter per second the GBT pointing performance degrades, principally due to excitation of feedarm vibrations; up to 4.0 m/s, the pointing accuracy is still acceptable for 31 GHz observations. We reject individual observations with mean wind speeds<sup>5</sup> over 3 meters per second; we also reject individual observations with peak wind speeds over 5 meters

---

<sup>5</sup>The “mean” windspeed is the average of all 3 GBT weather stations over the scan; the “max” windspeed is the highest windspeed recorded by any of the 3 GBT weather stations during the scan.



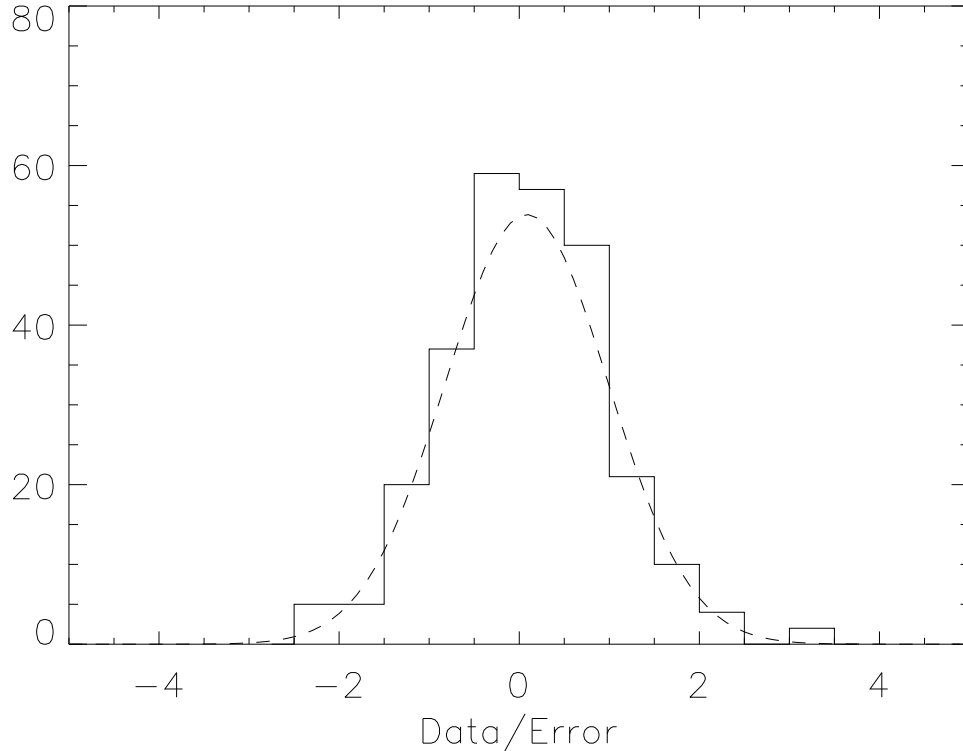


Fig. 7.— Distribution of blank-field measurements divided by their individual measurement noises estimated by Eq. 5. The dashed line shows the best fitting Gaussian which has  $\sigma = 0.91$ , close to the expected value of unity which would be obtained for perfectly estimated Gaussian noise; the noise values themselves varied by a factor of 4. Compare to the corresponding distribution of measurements for targeted NVSS sources in the survey, Figure 6.

per second. Every half hour (during the day) to 45 minutes (at night), the telescope pointing and focus is updated from observations of a nearby calibrator. Science program observations that for whatever reason are not preceded by a successful peak and focus correction within these periods of time are also rejected. There were no GBT data for which the sun or the moon were closer than 10 degrees away. The data filters are summarized in Table 1.

To check the effectiveness of our pointing update criteria we consider the ratio  $r$  of measured flux density in the 38 GHz band to that measured in the 31 GHz band for all sources detected at  $4\sigma$  or greater. The flux density measured in the high frequency band will fall more for a given pointing offset than will the lower frequency band. For the dataset as a whole  $r = 0.84 \pm 0.03$ , where the uncertainty is the error in the mean assuming Gaussian statistics from the RMS of the distribution. From the spectral index analysis of § 5.1 we calculate an expected  $r = 0.83 \pm 0.04$ ,

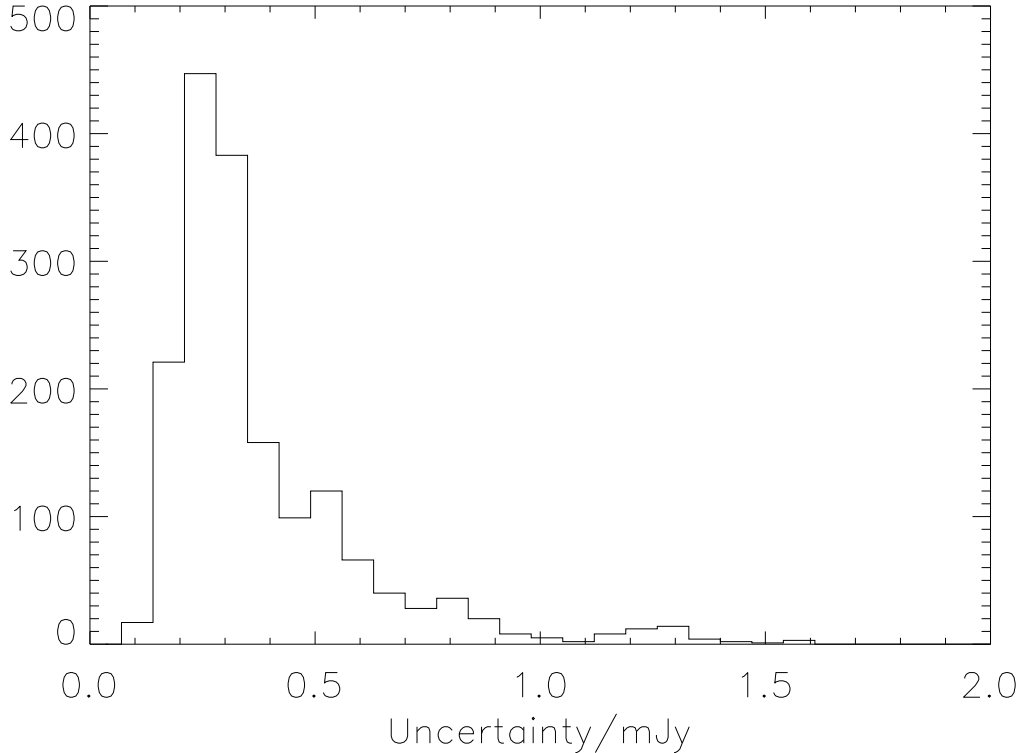


Fig. 8.— Distribution of estimated measurement errors in the GBT survey.

where the error bar in this case is the RMS of the distribution (indicating its intrinsic width) predicted by our Maximum Likelihood spectral index distribution under the assumption of a single power-law extrapolation. Note that selecting  $4\sigma$  detections will bias  $r$  slightly high relative to the full distribution. Splitting the data into two halves based on the time since the last pointing calibration, the data with more recent corrections has an average flux density ratio of 0.84, while data with less-fresh pointing corrections have an average flux density ratio of 0.83, indicating that there is no significant change in the telescope pointing between pointing checks. Similarly the daytime data have  $r = 0.83$  and the night-time data  $r = 0.84$ , indicating that on average the thermal effects prevalent during the day do not significantly affect the telescope pointing. The  $\Delta r = 0.01$  differences seen correspond to average radial pointing offsets of  $2''$  or 2% gain effects; a 10% loss in gain overall, if caused by a pointing offset, would correspond to  $\Delta r = 0.05$  (a  $4''.6$  radial offset). Note that this test is sensitive to any errors which causes relative changes in observed power across the receiver band. For instance, variations in the Ruze-equivalent RMS deviation of the telescope surface from a perfect paraboloid scale as  $\exp(-(4\pi\epsilon/\lambda)^2)$  and will, in a similar manner, affect the 38 GHz channel more than the 31 GHz channel.

To further check the accuracy of our noise estimate we make use of the fact that in the course of the survey 50 weak ( $s_{31} < 15$  mJy) sources were observed more than once; we select weak sources in order that the effect of gain errors, which can be correlated between observations, not be a dominant effect. In all there are 122 such observations. Subtracting the per-source means from each we calculate a  $\chi^2_\nu = 0.95$  for  $\nu = 72$ . The probability to exceed this by chance is 59%.

#### 4.5. The Effect of Finite Source Size

While most radio sources are compact compared to the GBT and OVRO beams, a handfull will be sufficiently extended that flux density will be lost in targetted observations. On angular scales at which the GBT begins to lose flux density ( $\sim 10''$ ) most of the extended emission seen in extragalactic sources originates in radio jets with a synchrotron spectrum  $\propto \nu^{-0.6}$  to  $\nu^{-1}$  (Laing & Peacock 1980; Dennett-Thorpe et al. 1999); the 31 GHz emission is dominated by the compact, flatter-spectrum cores. Consider for example that the NVSS at 1.4 GHz, with a  $45''$  (FWHM) beam find 20% of sources to be resolved, while 9C at 15 GHz, with a  $25''$  FWHM beam, finds only 9% of sources to be detectably resolved (Waldram 2008). Consequently we expect that most of the flux density in the 31 GHz sky will be in compact sources which are accurately measured by the GBT. Attempts to determine the lost flux at different observing frequencies need to account for this spectrum-morphology correlation.

The CBI data themselves do not have sufficient angular resolution or flux density sensitivity to make useful statements about 31 GHz source morphology: for instance, only 3 sources identified by NVSS as extended are detected in the CBI maps. Two of these are a pair separated by  $\sim 1'$  which the CBI data cannot distinguish these as separate components, likely indicating that the 31 GHz flux density is dominated by a single, more compact component. The remaining source shows a marginally significant reduction in  $\chi^2$  for a resolved Gaussian model in comparison to a point source model ( $\Delta\chi^2_\nu = -6 \times 10^{-4}$  for 14330 DOF).

We can however test for lost flux in the total dataset. To set aside the *most* extended sources, NVSS sources with useful GBT measurements were divided into two groups— those resolved by NVSS and those not resolved by NVSS— and from these groups two CBI visibility templates (actu-

Filter	Criterion	fraction of data passed
Wind	$\max < 5.0\text{m/s}$ , $\text{mean} < 3.0\text{m/s}$	79%
$\langle\chi^2_\nu\rangle$	$< 1.4$	54%
Pointing & Focus Updates	within 30 (day) or 45 (night) minutes	86%
Total		39%

Table 1: Summary of GBT data filters. For individual tests the fraction of the total dataset passed is shown; since there are correlations between the filtered variables the filters are not statistically independent.

ally, gridded estimator templates) were constructed. We fit for a scale factor  $S_{GBT} = f \times S_{CBI}$  for each template using the CBI visibility data in aggregate. For sources unresolved by NVSS we find  $f = 0.96 \pm 0.04$ , arguing that there is no systematic bias between the flux density scales and that there is no significant degree of source extension that is not detected by NVSS. We can make a complementary estimate of lost flux in the NVSS-compact sources using the higher-resolution ATESP 1.4 and 5 GHz surveys (Prandoni et al. 2000, 2006). These are matched-resolution ( $10''$ ) imaging surveys of  $1 \text{ deg}^2$ , complete to  $\sim 0.5 \text{ mJy}$ . With the 1.4 to 5 GHz spectral indices Prandoni et al. (2006) report on the 131 source spectral index sample, we extrapolate the 1.4 GHz flux densities to 31 GHz. The Gaussian component sizes at 5 GHz (or 1.4 GHz where 5 GHz fits are not reported) are convolved with a  $24''$  FWHM beam to determine the peak surface brightness, which is the flux density which would be measured in a targetted observation by the GBT. We find that 97% of the total 31 GHz flux density is recovered; 99% of the quantity  $\sum_i S_{31,i}^2$  is recovered. The latter is the better indicator of the impact of lost flux on the 31 GHz sky variance (CBI statistical point source correction). Since on average source spectral will steepen towards higher frequency and tend to be more compact than at 5 GHz, this is a lower limit to the fraction of recovered flux.

Fitting for a CBI/GBT scale factor using only the NVSS-*resolved* sources yields  $f = 1.18 \pm 0.10$ . The larger error bar in this is consistent with the (smaller) number of extended sources in comparison to the number of NVSS-compact sources. While there is some indication of lost flux in the NVSS-resolved sources, we find that excising the extended sources from the spectral index analysis of § 5.1 does not significantly change the spectral index PDF or final result for the statistical correction. This is consistent with the expectation that the 31 GHz sky variance is dominated by the flat, compact sources.

Except for a few isolated examples the OVRO measurements lose a negligible amount of flux even assuming the 1.4GHz morphology pertains at 31 GHz.

#### 4.6. Confusion

Since the angular resolution of the GBT and, especially, OVRO surveys are comparatively low ( $24''$  and  $1'.3$ , respectively) chance superpositions of radio sources will occasionally occur and must be considered. To assess the effects of source confusion we combined the OVRO and GBT catalogs, giving precedence to GBT measurements where present, and selected  $3\sigma$  or greater detections. To this we added the NVSS sources with 1.4 GHz flux densities  $> 3.4 \text{ mJy}$  and multiplied their flux densities by 0.1 (the mean ratio of  $S_{31}$  to  $S_{1.4}$  determined from the Maximum Likelihood analysis of § 5.1), thereby obtaining our best estimate of the point sources 31 GHz sky in the regions observed. We call this our “reference” catalog.

Consider that we have a set of  $N_{obs}$  potentially mutually confused measurements  $S_{obs,i}$  and seek to determine the true flux densities  $S_{T,i}$  of the targetted sources in the presence of a number of other contributing  $N_{est}$  sources for which we have no measurements, but only some uncertain

flux density estimates  $S_{est,j}$ . These quantities are related by

$$\begin{pmatrix} S_{obs,1} \\ S_{obs,2} \\ \dots \\ S_{obs,Nobs} \end{pmatrix} = \begin{pmatrix} B_{11} & B_{12} & \dots & B_{1,Nobs} \\ B_{21} & B_{22} & \dots & B_{2,Nobs} \\ & \dots & & \\ B_{Nobs,1} & \dots & & B_{Nobs,Nobs} \end{pmatrix} \begin{pmatrix} S_{True,1} \\ S_{True,2} \\ \dots \\ S_{True,Nobs} \end{pmatrix} + \dots \quad (6)$$

$$\begin{pmatrix} B_{11} & B_{12} & \dots & B_{1,Nest} \\ B_{21} & B_{22} & \dots & B_{2,Nest} \\ & \dots & & \\ B_{Nobs,1} & \dots & & B_{Nobs,Nest} \end{pmatrix} \begin{pmatrix} S_{est,1} \\ S_{est,2} \\ \dots \\ S_{est,Nest} \end{pmatrix}$$

where the  $B_{ij}$  is the beam weight that source  $j$  contributes to observation  $i$ , for a Gaussian beam

$$B_{ij} = \exp\left(-\frac{|\vec{x}_i - \vec{x}_j|^2}{2\sigma_{beam,i}^2}\right) \quad (7)$$

for an observation pointed at  $\vec{x}_i$  and a source at  $\vec{x}_j$ .  $\sigma_{beam,i}$  is the Gaussian beam width for measurement  $i$ , potentially different for different measurements if the data come from different telescopes as is the case here. This is a straightforward system of  $N_{obs}$  equations in  $N_{obs}$  unknowns.

We must also account for our off-source (or reference) beam positions. Due to our position-nodded beam-switching observing strategy, and the fact that the beamswitching occurs in azimuth, the reference (off-source) beams sweep out arcs on the sky giving a greater chance of encountering a second source; but tracking over a range of parallactic angles will cancel this effect on average. The OVRO data, with observations of a given source spread over many days or even months, sample a wide range of parallactic angles. Consequently for the OVRO data we use the average reference beam arcs in calculating the  $B_{ij}$ . The GBT data, in contrast, typically have a single measurement at a well-defined parallactic angle for a given source.

Using the reference catalog we scan the full set of OVRO observations and identify those for which the sum of the absolute values of beam-weighted confusing source flux densities in the reference catalog amounts to more than half the measurement error for that source. We solve Eqs. 7 for this subset of observations and use the corrected values in the catalog; revised uncertainties are also calculated by propagating the measurement errors, assuming  $\sigma(S_{est}) = S_{est}$  for the non-measured sources (determined from the distribution of  $S_{31}/S_{1.4}$  of § 5.1). For the OVRO data this affects 1.3% of the data.

Owing to the smaller beam size and beam throw the level of source confusion in the GBT data is much lower. Using the reference catalog only two observations are significantly confused. As a more stringent test we select all observations for which *any*  $S_{1.4} > 3.4$  mJy source falls within the pattern swept out by the GBT beams (including the regions between the A and B beams for each observation), amounting to 7% of the observations in all. For these observations we allow an extra flux density parameter associated with the confusing source in the fit (Eq. 4). In no case did this make a difference more than half of the thermal noise error bar.

#### 4.7. Source Catalogs

The full set of OVRO observations is presented in Table 2, and the GBT survey results are presented in Table 3. Reported error bars include a 10% RMS gain uncertainty for GBT and 5% RMS gain uncertainty for OVRO. Sources detected at greater than  $4\sigma$ , considering thermal noise only, are marked. In all 3165 sources were observed. The GBT catalog contains 1490 sources. Of the 2315 useful OVRO observations many of the non-detections (and a few detections) are superceded by more sensitive GBT observations; the OVRO catalog therefore contains data on 1675 sources. The detection rate of the OVRO measurements is 11%, and that of the GBT measurements 25%. In all 18% of sources are detected at 31 GHz.

Also included in the table are the 1.4 GHz flux densities and source sizes from the NVSS catalog, and a flag (“C”) to indicate which observations have been corrected for the effects of source confusion in either the main or reference beams.

### 5. Interpretation

#### 5.1. Spectral Index Distribution from GBT, OVRO, and NVSS Data

In order to determine the contribution of radio sources below the NVSS completeness limit to the sky variance measured by 31 GHz CMB experiments such as the CBI, it is necessary to understand the 1.4 to 31 GHz spectral index distribution — or equivalently, the probability density function (PDF) of  $S_{31}$  given  $S_{1.4}$ . The data from the survey presented in this paper are the best currently available for this purpose. Since sources detected at 31 GHz (15% of the sample as a whole) are preferentially flat-spectrum, it is necessary to include non-detections in this analysis to obtain an unbiased result. Because we have estimates of the low-frequency flux densities of these sources and of the 31 GHz measurement noise, these non-detected sources will impose constraints on the spectral index distribution. We adopt a Bayesian Maximum Likelihood approach.

We wish to find the spectral index distribution that maximizes the likelihood of measuring the observed 31 GHz flux densities given their observed 1.4 GHz NVSS flux densities. The general form of the likelihood of measuring 31 GHz flux density  $S_{31,obs}$  given 1.4 GHz flux density  $S_{1.4,obs}$  is:

$$P(S_{31,obs}|S_{1.4,obs}) = \int \int P(S_{31,obs}|S_{31,T}) P(S_{31,T}|S_{1.4,T}) P(S_{1.4,T}|S_{1.4,obs}) dS_{31,T} dS_{1.4,T} \quad (8)$$

integrating over the unknown  $S_{31,T}$  and  $S_{1.4,T}$ , and with the (unknown) 1.4-31 GHz spectral index function  $P(S_{31,T}|S_{1.4,T})$ . We can rewrite the likelihood in terms of flux density ratios and use the fact that the measurement errors are uncorrelated to get:

$$P\left(\frac{S_{31,obs}}{S_{1.4,obs}}\right) \propto \int dS_{31,T} P(S_{31,obs}|S_{31,T}) \int P\left(\frac{S_{31,T}}{S_{1.4,T}}|S_{1.4,T}\right) P\left(\frac{S_{1.4,T}}{S_{1.4,obs}}\right) dS_{1.4,T} \quad (9)$$

Name	RA/J2000	Dec/J2000	S30	E(S30)	S(1.4)	E(S1.4)	Maj	Min	D	C
085057-0150	08:50:57.06	-01:50:38.6	5.30	1.90	46.90	1.50	0.0	0.0		
085101-0509	08:51:01.80	-05:09:52.9	3.00	3.40	36.30	1.20	0.0	0.0		
085103-0303	08:51:03.94	-03:03:35.5	2.00	2.20	17.80	1.40	71.4	0.0		
085118-0419	08:51:18.93	-04:19:10.3	-3.13	2.81	62.70	2.30	15.3	0.0	*	
085121-0418	08:51:21.49	-04:18:25.7	11.74	2.75	66.00	2.40	45.5	0.0	*	*
085127-0156	08:51:27.01	-01:56:09.3	4.00	5.00	18.70	1.00	22.7	0.0		
085130-0155	08:51:30.58	-01:55:49.4	-4.30	3.80	22.70	0.80	0.0	0.0		
085135-0150	08:51:35.60	-01:50:44.9	5.80	2.70	55.20	1.70	0.0	0.0		
085137-0405	08:51:37.67	-04:05:00.7	3.40	3.30	27.40	0.90	0.0	0.0		
085138-0451	08:51:38.97	-04:51:23.8	14.20	3.20	78.40	2.40	0.0	0.0	*	
085141-0424	08:51:41.73	-04:24:35.6	2.80	2.10	13.70	0.60	0.0	0.0		
085149-0314	08:51:49.11	-03:14:57.0	0.70	2.50	81.40	2.90	29.8	0.0		
085157-0408	08:51:57.40	-04:08:01.2	-0.10	1.80	17.30	0.70	0.0	0.0		

Table 2: Excerpt of OVRO 40-m survey results. Positions and 1.4 GHz flux densities are from NVSS. Columns are: NVSS name; Right Ascension (J2000); Declination (J2000); 30 GHz flux density and uncertainty; NVSS integrated flux density and uncertainty; NVSS Major axis in arcseconds (0.0 indicates no detected size); NVSS minor axis in arcseconds. A flag in the “D” column indicates a  $4\sigma$  detection, and a flag in the “C” column indicates that a confusion correction has been performed by the method described in the text. The full version of this table is available on line.

Name	RA/J2000	Dec/J2000	S30	E(S30)	S(1.4)	E(S1.4)	Maj	Min	D	C
024033-0432	02:40:33.53	-04:32:47.5	0.37	0.32	5.50	0.50	0.0	0.0		
024038-0425	02:40:38.89	-04:25:54.5	0.81	0.31	4.00	0.50	0.0	0.0		
024055-0428	02:40:55.18	-04:28:36.4	0.34	0.30	4.50	0.50	0.0	0.0		
024108-0422	02:41:08.83	-04:22:51.4	5.32	0.30	6.90	0.50	0.0	0.0	*	
024111-0425	02:41:11.61	-04:25:21.4	1.23	0.30	26.80	0.90	0.0	0.0	*	
024119-0421	02:41:19.39	-04:21:44.4	2.71	0.33	17.20	0.70	0.0	0.0	*	
024129-0003	02:41:29.53	-00:03:27.4	-2.40	1.19	4.70	0.50	0.0	0.0		
024137-0039	02:41:37.85	-00:39:19.4	0.56	0.61	14.60	0.60	0.0	0.0		
024144-0416	02:41:44.17	-04:16:48.0	5.88	0.32	84.50	3.30	32.6	16.5	*	
024146-0025	02:41:46.15	-00:25:01.7	0.89	0.60	5.70	0.50	0.0	0.0		
024153-0105	02:41:53.70	-01:05:43.3	0.15	0.24	3.40	0.50	0.0	0.0		
024204-0053	02:42:04.56	-00:53:33.7	0.26	0.24	5.60	0.50	0.0	0.0		
024206-0419	02:42:06.51	-04:19:02.2	0.90	0.33	21.10	1.10	20.9	0.0		

Table 3: Excerpt of GBT 31 GHz survey results. Columns are as in Table 2.

The outer integral is a convolution with the 31 GHz (OVRO and GBT) measurement error distribution; the inner integral folds the flux density ratio through the 1.4 GHz measurement error distribution, including a Malmquist-bias correction in the  $P(S_{1.4,obs}|S_{1.4,T})$  which assumes differential source counts of the form  $S^{-1.66}$ . Since the measurements of each source are independent, the total log-likelihood is the sum of the log-likelihoods for individual sources, and evaluating the likelihood reduces to (efficiently) evaluating the individual PDFs for all the 31 GHz flux density measurements (OVRO and GBT). Several points should be noted:

1. Under the assumption (to be checked) that the  $\frac{S_{31,T}}{S_{1.4,T}}$  distribution is independent of the 1.4 GHz flux density over the range of interest, we can take  $P\left(\frac{S_{31,T}}{S_{1.4,T}}|S_{1.4,T}\right) \rightarrow P\left(\frac{S_{31,T}}{S_{1.4,T}}\right)$  *i.e.* the distribution is the same for all sources and needs to be calculated only once.
2. For computational efficiency, we pre-calculate the FFT of the inner integral,  $P\left(\frac{S_{31,T}}{S_{1.4,obs}}\right)$  for a range of 1.4 GHz signal-to-noise values at each likelihood step, then linearly interpolate between these values for a given source.
3. Calculating  $P(S_{31,obs}|S_{1.4,obs})$  requires convolving  $P(S_{31,true})$  with the 31 GHz noise. We use the fact that we wish to evaluate  $P(S_{31,observed})$  only at the actual observed flux density to speed up the convolution. Because we calculate the Fourier transform of  $P(S_{31,true}|S_{1.4,observed})$  in the previous step, the convolution with the (Gaussian) 31 GHz noise is an analytic multiplication. We evaluate the back-transform only at the two FFT points bracketing the observed flux density, then linearly interpolate between them. This saves us from having to do a full FFT for each source, with computational load reduced from  $N \log(N)$  to  $2N$ .
4. Because differences in log-likelihood are meaningful, the maximum-likelihood process naturally produces meaningful errors in the flux density distribution that fold in both the measurement errors and the uncertainty due to the finite number of sources measured.

We parameterize  $\frac{S_{31,T}}{S_{1.4,T}}$  with a set of evenly spaced points in the frequency spectral index  $\alpha$ , and do a piecewise-Hermite cubic polynomial interpolation through them, padded with zeros on either side. The Hermite interpolation is similar to a spline, but has two key advantages: the interpolation is always local so it never rings, and the function values between interpolation points are always bracketed by the function values at points. So, as long as our model points stay non-negative, the interpolated PDF will also be strictly non-negative.

To measure the the PDF and its uncertainty, we use the publicly available Markov-Chain Monte-Carlo (MCMC) code COSMOMC (Lewis & Bridle 2002) adapted for use with a generic likelihood function. The MCMC algorithm draws samples a multi-dimensional parameter space, in this case the space of  $N_{bin}$  parameters representing the spectral index distribution, with a specified distribution, in this case the likelihood of the parameters given the data. This procedure permits easy evaluation of the uncertainties and covariances in parameters of interest (the spectral index distribution); it also makes evaluating the uncertainties and covariances in functions of these



parameters quite straightforward (*e.g.*, § 5.2). The code is run on 8 nodes of a Beowulf cluster, typically requiring about half a day. We use a set of bins with centers between -1.6 and +0.95 in  $\alpha$  with a bin size of 0.15. To check the sensitivity of results to the choice of binning, we also repeat the Maximum Likelihood analysis with the bin centers staggered by half a bin.

The marginalized posterior distributions of the parameters of the spectral index PDF are shown in Figure 9. This is our best description of 1.4 to 31 GHz source spectral indices. Table 5 summarizes the results in binned form, calculated from 100,000 samples from the MCMC chains. We find that 8.8% of sources have spectral indices flatter than  $\alpha > -0.5$  and 0.9% have inverted spectral indices,  $\alpha > 0$ .

As a check we split the input by NVSS flux density and estimated the spectral index distribution for each of the bright and faint samples separately, with results shown in figure 9. At low flux densities the faint subsample provides little constraint on the spectrally steep end of the distribution, reflected by large error bars in that regime. The consistency of the subsamples supports the assumption that the spectral index distribution is constant over the range of flux densities of interest. To further assess the robustness of our conclusions we re-ran the spectral index distribution chains varying the assumed noise level of the OVRO and GBT data by  $\pm 20\%$  and excised potentially confused sources. Results are summarized, along with the nominal case, in Table 4. Shown are the mean spectral index and its RMS, the fraction of sources with flat or rising spectra, the mean 31 to 1.4 GHz flux density ratio, and the mean-square flux density ratio, which is more indicative of the variance of the source population.

## 5.2. 31 GHz Source Counts

We have estimated the 31 GHz counts by drawing flux densities between  $50 \mu\text{Jy}$  and  $1 \text{ Jy}$  from the Hopkins et al. 1.4 GHz counts and extrapolating them to 31 GHz with samples from our 1.4 to 31 GHz PDF. Over the range  $0.3 \text{ mJy} < S_{31} < 20 \text{ mJy}$  the counts follow a power law

Test:	Noise $\times 0.8$	Nominal	Noise $\times 1.2$
$f_{\alpha \geq 0.0}$	$1.24 \pm 0.15\%$	$1.17 \pm 0.15\%$	$0.92 \pm 0.18\%$
$\langle S_{31}/S_{1.4} \rangle$	0.117	0.111	0.101
$\langle (S_{31}/S_{1.4})^2 \rangle$	0.099	0.092	0.084
$\langle \alpha \rangle$	-0.911	-0.917	-0.925
$\langle \sigma_\alpha \rangle$	0.336	0.311	0.292

Table 4: Results of tests of the spectral index distribution estimate. Shown are the fraction of rising spectrum sources, the mean flux density ratio (1.4 to 31 GHz), the mean of the square of the flux density ratio (which is directly relevant to the residual source variance), and the mean spectral index for a range of perturbed GBT and OVRO noise levels, and for the case where all measurements potentially affected by confusion are excised.

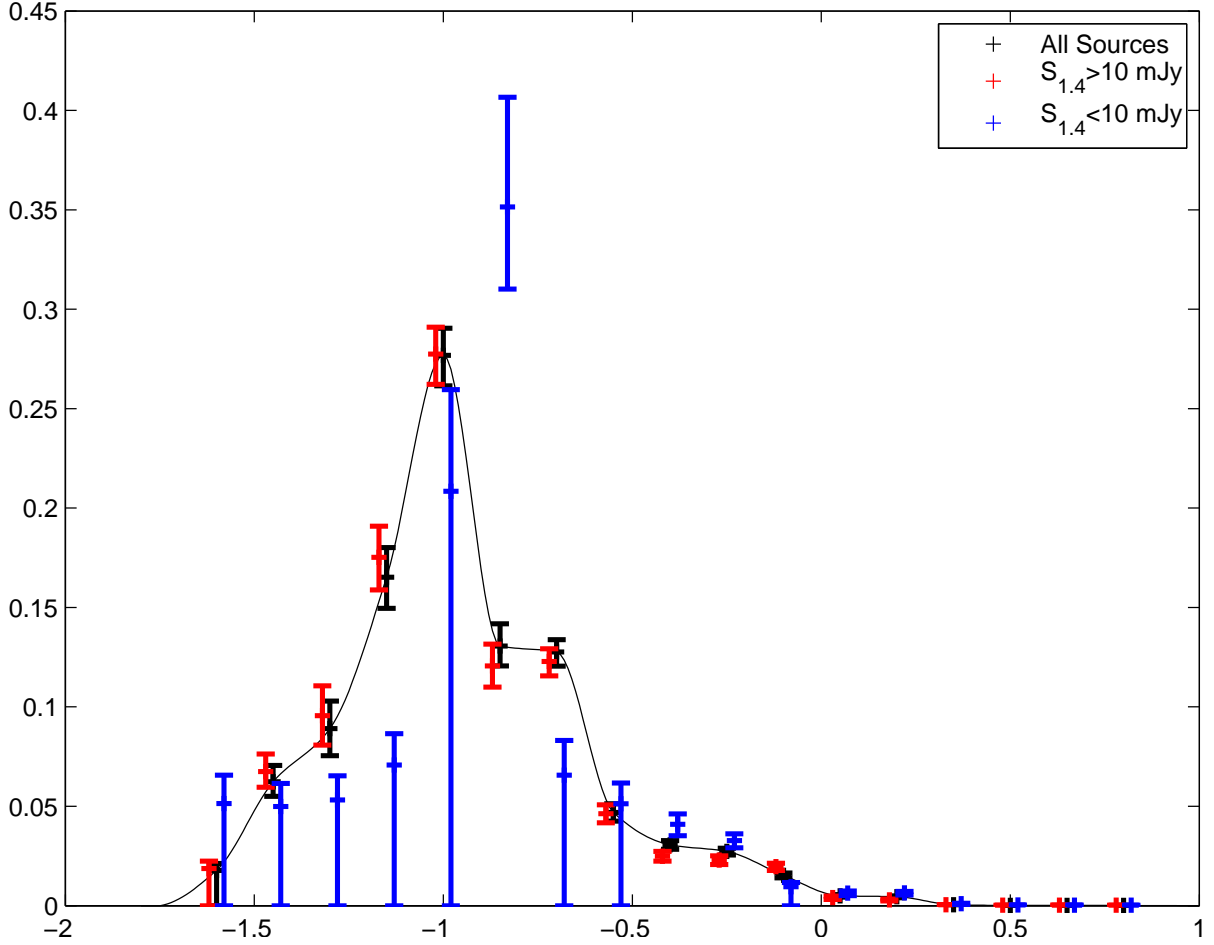


Fig. 9.— 1.4 to 31 GHz spectral index distribution determined from GBT, OVRO, and NVSS data. Also shown are determinations for bright and faint NVSS subsamples. Error bars are the 1-parameter marginalized  $1\sigma$  uncertainties for the individual points parameterizing the spectral index PDF.

Spectral Index	$f/\%$
-1.7	0.194630
-1.6	1.02
-1.5	2.96
-1.4	5.62
-1.3	6.43
-1.2	8.57
-1.1	14.8
-1.0	16.4
-0.9	12.2
-0.8	9.11
-0.7	7.45
-0.6	4.86
-0.5	2.73
-0.4	1.97
-0.3	1.78
-0.2	1.59
-0.1	1.01
0.0	0.45
0.1	0.32
0.2	0.25
0.3	0.10
0.4	0.015
0.5	$6.99 \times 10^{-03}$
0.6	0.01
0.7	$9.00 \times 10^{-3}$
0.8	$3.99 \times 10^{-03}$
0.9	$9.98 \times 10^{-04}$

Table 5: GBT/OVRO+NVSS 1.4 to 31 GHz spectral index distribution.

$dN/dS \propto S_{31}^{-1.8}$ , with a normalization at 1 mJy of  $S^{5/2} dN/dS = 1.18 \pm 0.05 \text{ Jy}^{-1.5} \text{ sr}^{-1}$ . Directly summing the simulated source populations gives an integrated source count of

$$N(> S_{31}) = (16.74 \pm 0.42) \times (S_{31}/1\text{mJy})^{-0.80 \pm 0.01} \text{ deg}^{-2}. \quad (10)$$

As shown in Figure 10 our 31 GHz counts compare favorably with other measurements (Mason et al. 2003; Cleary et al. 2005; Kovac et al. 2002). We can apply this procedure over an arbitrary range of flux densities but it is only valid over the range that our spectral index PDF is valid. Conservatively we take this to be 0.5 mJy to 10 mJy, although the consistency of our counts with direct measurements at higher flux densities is excellent. The GBT counts have a similar slope to the model of de Zotti et al. (2005), although the normalization of the GBT counts is 15% lower in the 1 – 10 mJy range. The Toffolatti et al. (1998) counts are substantially higher than both in this range. Below 0.3 mJy the 31 GHz counts in our model show a weak turn-up due to the sub-mJy population but the precise location and magnitude of this turn-up depends on the assumed spectra of these sources (see § 5.3.2). The error bars on the result are determined using the set of MCMC-sampled spectral-index PDFs.

### 5.3. The Effect of Unresolved Sources on CBI Measurements

#### 5.3.1. Simulations

Point sources are the largest astrophysical foreground in the CBI data, and are especially critical at high- $\ell$ . An accompanying paper (Sievers et al. in prep.) presents the power spectrum from 5 years of CBI observations. We have used the results of GBT and OVRO 40-m measurements presented here to quantify the impact of discrete sources on the power spectrum. As discussed in § 1 there are two distinct classes of sources to be treated: those which are individually known and identified from imaging surveys (NVSS); and sources in our fields not detected in any survey, but expected to be present based on source counts extending below the survey detection limits in other fields. Very conservatively, all known sources are projected out of the CBI dataset; the efficacy of this procedure is quantified in Sievers et al. (in prep.). Our task, and the fundamental aim of this paper, is to quantify the statistical contribution of the fainter sources. This population is a *low-frequency selected population* (sources below the NVSS detection threshold), and we must calculate the variance of its sky brightness at 31 GHz.

To do this we have undertaken an extensive suite of simulations. Essentially we create realistically constrained realizations of the sub-NVSS populations and run these realizations through the full CBI power spectrum pipeline; the procedure is schematically illustrated in Figure 12. We first draw 1.4 GHz populations down to 0.2 mJy using a power-law fit to the FIRST counts (White et al. 1997) between 2 and 100 mJy, representing the dominant contribution of mJy-level AGN. The contribution of sources below 1 mJy at 1.4, which likely have different spectral indices than the mJy AGN, is considered in § 5.3.2. We then simulate NVSS observations of these source realizations,

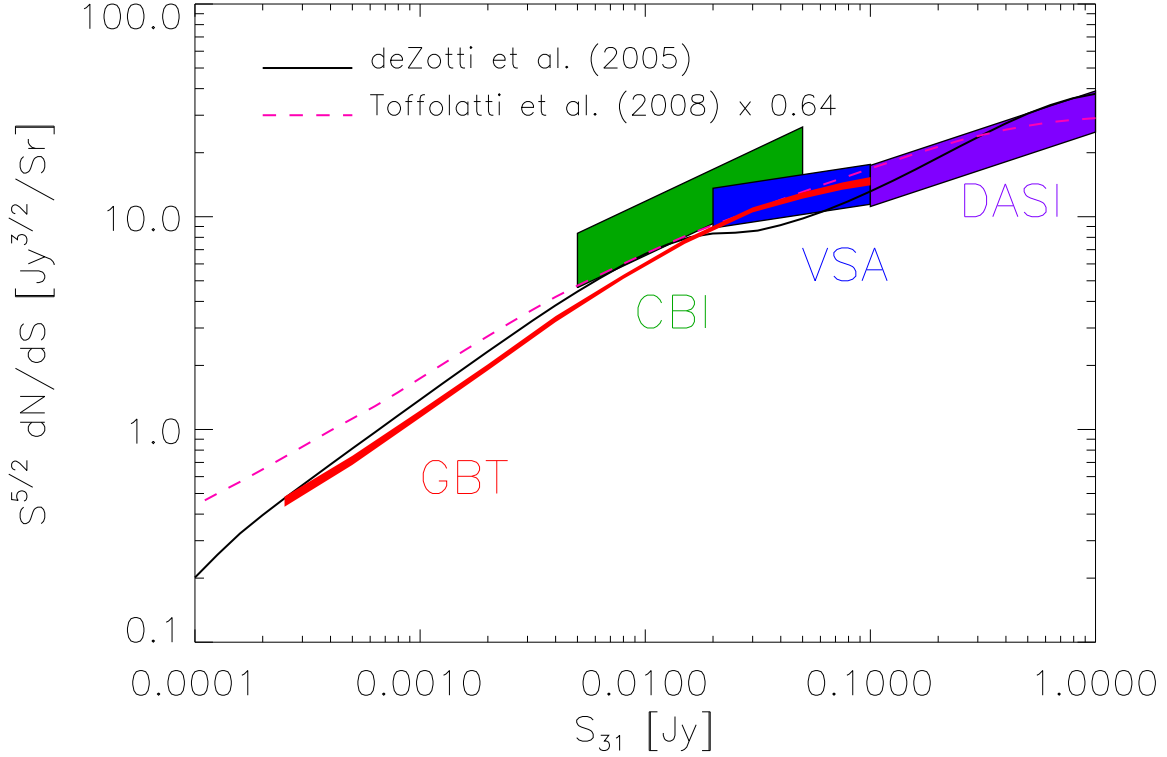


Fig. 10.— 31 GHz source count measurements and models. CBI results are from Mason et al. (2003), VSA results from Cleary et al. (2005), and DASI results from Kovac et al. (2002). All data are at 31 GHz except for VSA, which is at 33 GHz. Also shown is the Toffolatti et al. (1998) 31 GHz model scaled down by a factor of 0.64 and the de Zotti et al. (2005) 33 GHz model. The GBT error box is from the Markov Chain analysis described in the text; other experiments’ errors are taken from the Poisson error in the count normalization.

adding Gaussian noise of 0.6 mJy. Any source that has an observed (noisy) flux density greater than our NVSS projection threshold of 3.4 mJy is then removed, leaving a realistic population of 1.4 GHz sources that would not have appeared in NVSS. The sources with 1.4 GHz flux densities fainter than 0.2 mJy (which we do not simulate) should only contribute about 2% of the total power from the sources fainter than 3.4 mJy, given the FIRST 2-100 mJy power-law slope of  $\frac{dN}{dS} = -1.66$ . We then draw one 1.4-31 GHz spectral index distribution from the Markov chains in § 5.1, with the assumption that the spectral index distribution is independent of 1.4 GHz flux density, and assign each source a spectral index drawn from the distribution. We then add the signal from these faint-source realizations to CMB+noise simulations of the CBI dataset. Since CBI detects no sources at 31 GHz not present in NVSS, we search the set of simulations for such orphan sources using the method described in Weintraub et al. (in prep.), and reject any realization where such

a source is found. There are a few (3-4)  $\sim 5 - \sigma$  features in the CBI maps that are marginally inconsistent with association with an NVSS source. We have followed these up with the GBT and do not detect any actual sources, which implies they are most likely simply noise fluctuations. The possibility still exists that these fluctuations are chance superpositions of multiple faint sources in the same CBI beam. The GBT could miss such a superposition if no individual source falls within the GBT’s much-smaller beam when pointed at the effective emission center. To account for this possibility, we carry out mock GBT observations on fluctuations in the simulated maps classified as orphan sources, and do *not* reject any simulations based on map fluctuations where the GBT would not have detected a source. This gives us a set of simulated source catalogs that are consistent with the observed 1.4-31 GHz spectral index distribution and the fact that CBI detects no orphan 31 GHz sources.

We create a total of 500 source simulations, 250 for each of the binnings in § 5.1 and subject them to the map test described above. In 215 of the 500 (the “clean” simulations), no source is detected in the simulated CBI maps. In 285 of them (the “dirty” simulations) one or more source is detected. We take the visibilities from the source simulations and run them through the full CBI pipeline, fitting an  $\ell^2$  model to them.

The resulting estimate of the CBI residual source contamination is shown in Figure 13. We find the mean signal from the clean simulations is  $0.036 \pm 0.014$  Jy<sup>2</sup>/Sr, and that the mean signal from the dirty simulations is  $0.064 \pm 0.058$  Jy<sup>2</sup>/Sr. In particular, the dirty simulations have a tail to high power that the map test removes, also shown in Fig. 13. The maximum power in any of the 215 clean simulations is  $0.093$  Jy<sup>2</sup>/Sr, compared to  $0.43$  Jy<sup>2</sup>/Sr in the dirty simulations. There is no significant difference between the average statistical corrections of the clean simulations for the two binnings:  $0.037 \pm 0.016$  and  $0.036 \pm 0.012$  Jy<sup>2</sup>/Sr. The non-gaussian nature of the distribution is substantial - the scatter in gaussian simulations with the same average power as the clean simulations is only  $0.0025$  Jy<sup>2</sup>/sr, a factor of 5.5 lower.

Our observed level is in good agreement with, though generally lower than, past measurements. Mason et al. (2003) found  $0.08 \pm 0.04$  Jy<sup>2</sup>/Sr, the value used in previous CBI analyses, based on Owens Valley 40-m measurements. The data in Cleary et al. (2005) predict a mean level of  $0.03$  Jy<sup>2</sup>/Sr.

We comment briefly on the nearly factor-of-two difference between the power in the clean and the dirty simulations. If instead of checking the maps made of the entire set of simulated sources, we instead check the flux density each source individually to see if it is above the CBI map noise level, the mean level of clean simulations and dirty simulations is much closer, with the cleans averaging 77% of the dirties, as opposed to 57%. The cleans in this case also have an appreciable tail to high flux density, in rare instances extending past  $0.2$  Jy<sup>2</sup>/Sr. The difference is that the map-based test is sensitive to near-superpositions (within the CBI beam) of faint flat or inverted spectrum sources, while the individual source flux density test is not. Thus the fact that no “new” 31 GHz sources are detected in the CBI maps amounts to a constraint on the inverted spectrum tail of the spectral

index distribution. Within the range of spectral indices allowed by the GBT & NVSS data, the primary means by which this constraint comes into play is not primarily by ruling out strongly inverted spectrum sources — these are already effectively constrained by the GBT data — but by constraining the sky density of chance superpositions of moderately inverted sources. Given the number density of low frequency radio sources on the sky and the CBI’s comparatively large (5′) beam, this is a significant constraint.

The fact that no non-NVSS sources are detected by the CBI+GBT indicates that the clean simulations correspond to the instance of sources in our real dataset. The full distribution of clean simulations is used in the CBI power spectrum analysis of Sievers et al. (in prep.). We note that even if the the map-based distinction between clean and dirty simulations is neglected, only 1% of instances of source populations give sufficient signal to equal or exceed the high- $\ell$  excess power seen at 31 GHz.

### 5.3.2. *The Contribution of sub-millijansky Galaxies*

Our simulations considered only the power-law-distributed source population which is seen at mJy levels and higher in low frequency surveys. We must also consider the contribution of fainter sources likely belonging to a different population and having different spectral properties. At 1.4 GHz flux densities under  $\sim 1$  mJy the source counts turn up due to the emergence of the high- $z$  starbursting galaxies (Windhorst et al. 1985, *e.g.*) — see Figure 11. We estimate the impact of this population by first considering source correction at low frequency. Explicitly integrating the source count of Hopkins et al. (2003) from  $50 \mu\text{Jy}$  to  $3.4 \text{ mJy}$  we find a total 1.4 GHz statistical source contribution of  $C_{src} = 0.86 \text{ Jy}^2 \text{ sr}^{-1}$ . We assume that the turn-up is due to a physically distinct population. Integrating the power law over this range gives  $0.72 \text{ Jy}^2 \text{ sr}^{-1}$ , thus, the contribution of the sources responsible for the turn-up in the counts below a millijansky is  $0.12 \text{ Jy}^2 \text{ sr}^{-1}$  at 1.4 GHz. This implies that *even if every single one of these sources had a flat spectrum between 1.4 and 31 GHz they would account for barely half of the small-scale power in excess of the CMB observed by CBI* of  $0.23 \text{ Jy}^2 \text{ sr}^{-1}$ . In contrast to this, observations of  $\mu\text{Jy}$  sources (Richards 2000) show typical spectral indices between 1.4 and 8 GHz of  $-0.8$ , consistent with the observed dominance of synchrotron in nearby starbursting galaxies (Yun & Carilli 2002; Condon 1992).

Assuming the same distribution of spectral indices as we have determined for mJy level radio galaxies we obtain a 31 GHz value  $C_{src} = 0.010 \text{ Jy}^2 \text{ sr}^{-1}$ , a small correction to  $0.036 \text{ Jy}^2 \text{ sr}^{-1}$  which we include in the analysis. de Zotti et al. (2005) also find that sub-mJy galaxies make a minor contribution in comparison to mJy level AGN.

It is possible that the sources responsible for the turn-up in the low frequency counts could have a high incidence of inverted-spectrum sources extending to 31 GHz thus contributing more to the high- $\ell$  source correction. Using simulations similar to those in § 5.2 with modified spectral index distributions we estimate that were these sources to have moderately inverted spectral ( $\alpha \sim 0.2$ )

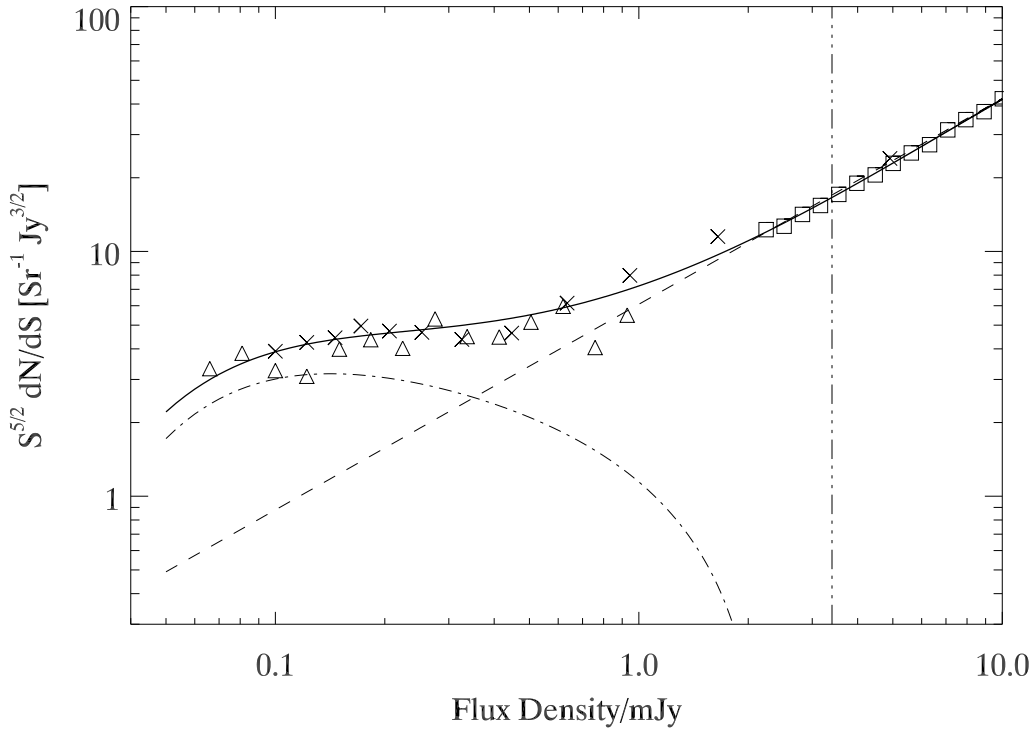


Fig. 11.— 1.4 GHz source counts. The solid line is the model of Hopkins et al. (2003) and triangles are their measurements in the Phoenix Deep Field; x’s are the source counts from the COSMOS field (Bondi et al. 2008); and squares are source counts from FIRST (White et al. 1997). The dashed line is a power-law fit to the FIRST source counts at flux densities fainter than 100 mJy and the dot-dash line is the excess of the full source counts over the power law form. The vertical dash-triple-dot line is the CBI projection threshold: the sources of interest are those to the left of this line. The power law behavior persists up to 100 mJy.

they would need to constitute 40% of the sub-mJy population in order to fully explain the CBI excess. Were they to have strongly inverted spectra ( $\alpha \sim 0.8$ ), 2% of the population would be required. In contrast, the GBT+OVRO surveys the most steeply inverted spectrum source had  $\alpha = 0.49$  and  $< 0.1\%$  of sources had  $\alpha > 0.3$ . Both cases would give rise to substantial enhancements (factors of 1.5 and 3 for the strongly and moderately inverted cases, respectively) enhancements of the 31 GHz source counts over those reported in § 5.2 in the 1 to 10 mJy range. Preliminary analysis of deeper 31 GHz GBT (Mason et al. in prep.) and ATCA (Taylor et al. in prep.) observations targeting a small sample of  $\sim 40$  sources with  $S_{1.4} \sim 1$  mJy indicates that the mean 1.4 – 31 GHz spectral index of these sources is comparable to that of the AGN population and that there is not a substantial population with inverted spectra continuing to 31 GHz.



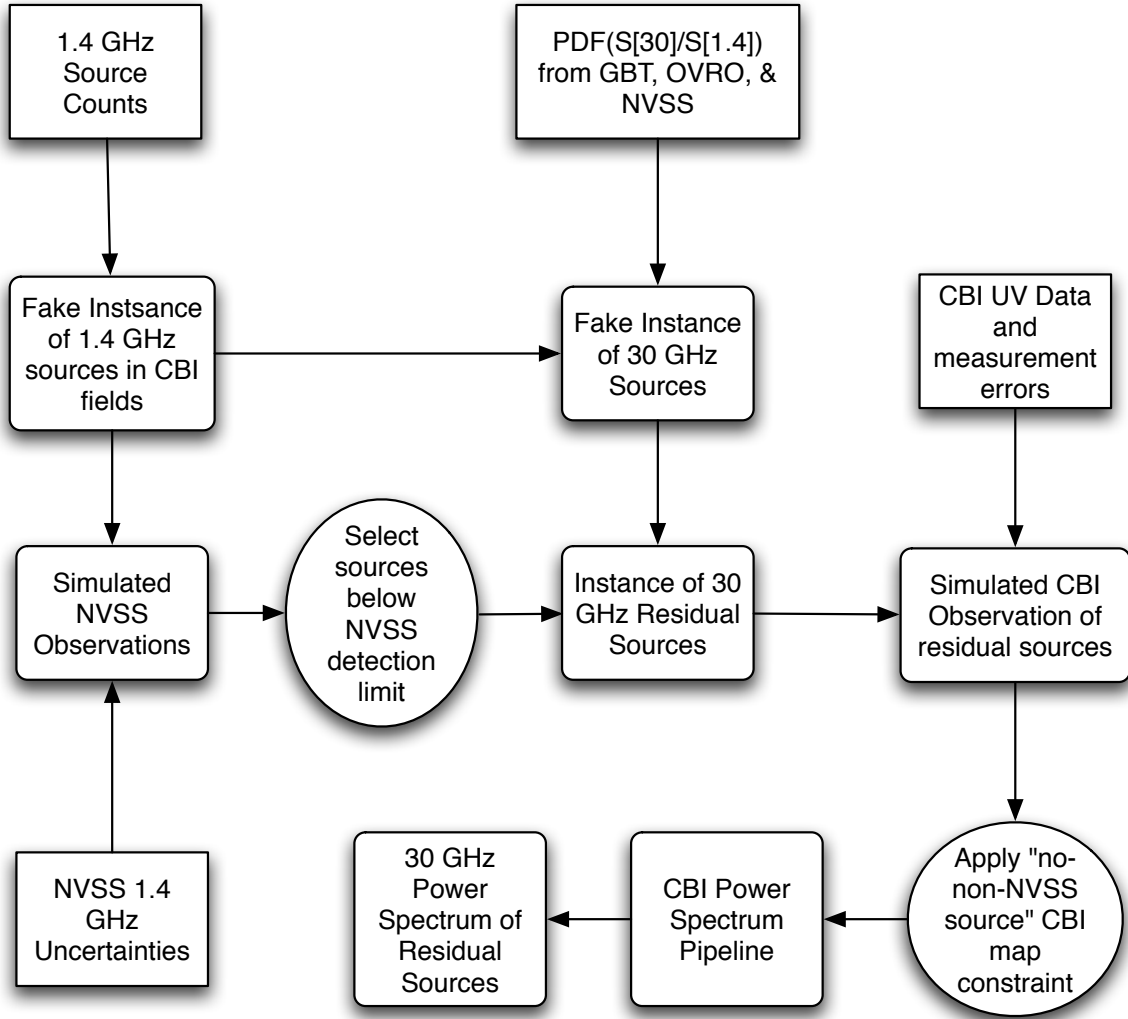


Fig. 12.— Schematic of the simulation pipeline we use to estimate the distribution of residual source power in the CBI power spectrum.

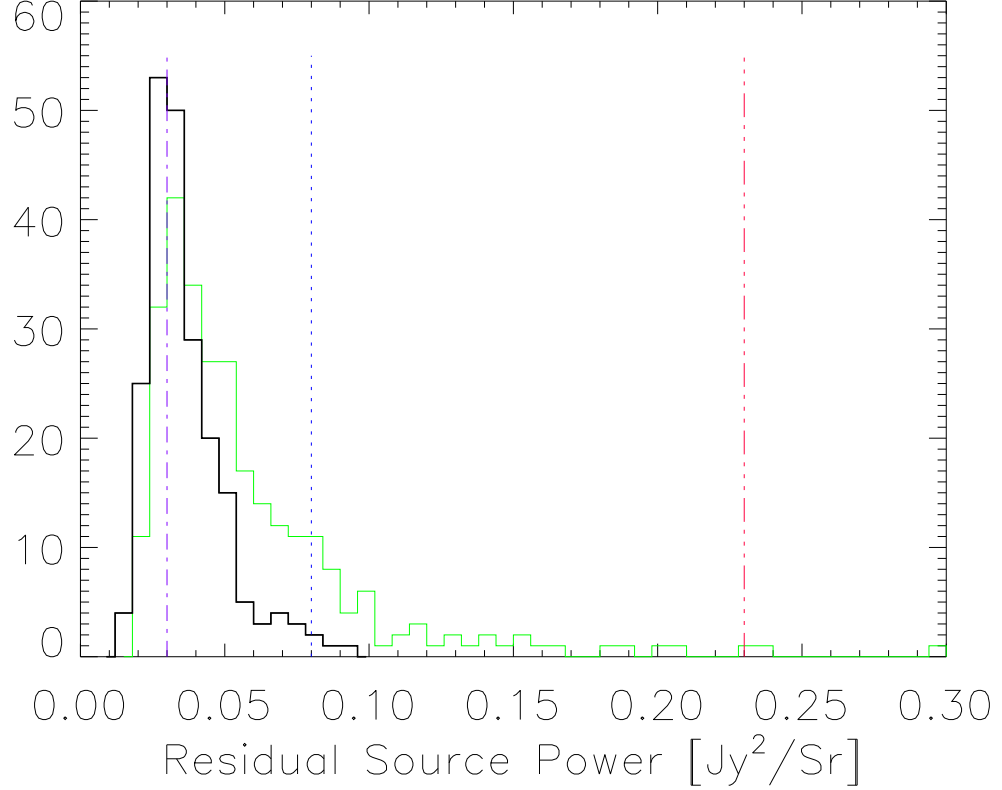


Fig. 13.— CBI residual source contamination, determined from low-frequency source counts plus GBT and OVRO 31 GHz information, via simulations described in the text. The heavy black line is the distribution for realizations with no non-NVSS sources seen in the 31 GHz (CBI) maps, corresponding to the actual CBI dataset. The light green distribution is for realizations which have one or more non-NVSS sources seen in the 31 GHz CBI maps. The residual source correction used prior to this work is shown as a dotted blue line; the dash-dot purple line is that calculated by Cleary et al. (2005) from VSA source counts at 31 GHz; and the red dash-triple-dot line is the level of source contamination needed to fully account for the power that CBI observes in excess of intrinsic CMB anisotropy (Sievers et al. in prep.).

### 5.3.3. Source Clustering

In addition to the Poisson or shot noise contribution of discrete sources to the power spectrum there will also be a contribution due to their spatial correlations, given by the second term of (Scott & White 1999; Oh et al. 2003)

$$C_{src} \propto \int_0^{s_{max}} ds s^2 \frac{dn}{ds} + \omega_\ell \left( \int_0^{s_{max}} ds s \frac{dn}{ds} \right)^2 \quad (11)$$

$$\propto \langle s^2 \rangle + \langle s \rangle^2 \omega_\ell \quad (12)$$

where  $\omega_\ell$  are the coefficients of the Legendre polynomial expansion of the discrete source angular correlation function (ACF)  $\omega(\theta)$ . The first term on the right hand side of this equation is simply the shot noise contribution which has already been considered in detail. Using the NVSS Blake & Wall (2002) find for mJy radio sources  $\omega(\theta) = 1.04 \pm 0.09 \times 10^{-3} \left( \frac{\theta}{deg} \right)^{-0.85}$  (Blake & Wall 2002), comparable in amplitude and slope to that of ordinary galaxies; for this ACF,  $\omega_\ell$  is  $\sim 10^{-5}$  over the range  $0 < \ell < 4000$ . From the 31 GHz flux density PDFs determined in § 5.1 we find  $\langle S_{31} \rangle^2 / \langle S_{31}^2 \rangle = 0.04$ , so at the faint flux densities relevant to our statistical correction clustering contributes less than one part in  $10^6$  to the total source power spectrum and is thus negligible. The sub-mJy sources, which have a substantial contribution from starbursting galaxies, could be more strongly clustered than mJy AGN. Applying the  $3\sigma$  upper limit of Webb et al. (2003) on the clustering amplitude of submillimeter galaxies to the sources lying above the AGN differential counts power law does not change the conclusion from the calculation.

### 5.3.4. Source Variability

Some sources exhibit significant time variability, with variability measures increasing to timescales of up to  $\sim 2$  years (Hughes et al. 1992). The effect of this will be to broaden our measurement of the apparent 1.4 to 31 GHz flux density ratio  $r(t_1 - t_2) = S_{31}(t_2)/S_{1.4}(t_1)$  over what would be observed in a commensal multi-frequency survey,  $r_0 = S_{31}(t_1)/S_{1.4}(t_1)$ . Provided the 31 GHz measurements are separated from the 1.4 GHz measurements by a period of time greater than the longest characteristic timescale for variations, our measured distribution of  $r$  will be a statistically fair description of  $S_{31}(t_3)/S_{1.4}(t_1)$  for other 31 GHz occurring at some time  $t_3$  also separated from  $t_1$  by greater than the longest characteristic timescale for variation. Considering that the 1.4 GHz NVSS observations were collected from September 1993 to October 1996, the CBI observations from November 1999 to April 2005, and the GBT observations from February to May of 2006, this will largely be the case. There could be a small number of variable sources with variability measures increasing beyond time spans of 10 years but compared to the sample as a whole these are rare and will have little impact on our results.

We note that while  $r$  is a fair sample to describe the CBI residual source power, extrapolations between frequencies other than 1.4 and 30 GHz will be biased. Even assuming that all sources

instantaneously have true power-law spectra, sources whose apparent spectral indices fluctuate flatwards due to variability make very different marginal contributions to the calculated sky variance at another frequency than those whose apparent spectral indices fluctuate steepwards.

## 6. Conclusions

By measuring the 31 GHz flux densities of a large sample of 1.4 GHz selected sources we have for the first time characterized the 31 GHz properties of a large sample of mJy-level radio galaxies. Crucially, our sample was large enough to accurately characterize the frequency of the rare inverted spectrum sources which can contribute significantly to the 31 GHz counts, and even more to the 31 GHz sky variance. We find that the majority of sources have steep spectral indices  $\alpha \sim -1$ , between 1.4 and 31 GHz, that the fraction of sources with  $\alpha > -0.5$  is  $\sim 9\%$ , and that the fraction with inverted spectral indices  $\alpha > 0$  is  $\sim 1\%$ . This has allowed us to greatly improve the accuracy with which we calculate the statical point source correction for the Cosmic Background Imager experiment. We find that the mJy-level (at 1.4 GHz) radio sources, mostly AGN, which dominate the CBI source correction typically contribute  $< 1/6$  of the signal seen by CBI in excess of intrinsic anisotropy at  $\ell > 2000$ . Exotic populations of faint inverted-spectrum sources not present at  $S_{1.4}$  of a few mJy can compromise these conclusions, but the requirements are extreme: 20% of  $S_{1.4} < 1$  mJy sources would need to have  $\alpha = 0.2$ , for instance, a factor of twenty more than is observed at mJy levels in this survey; or 2% of  $S_{1.4} < 1$  mJy sources would need to have  $\alpha = 0.8$ , while in this survey of 3165 sources only a single source was as steeply inverted as  $\alpha = 0.5$ . Both scenarios would imply enhancements of the 31 GHz source counts by at least 50% at 1 mJy.

It is worth noting several points in connection with these conclusions. First, it is essential to appreciate that the residual sources are fundamentally selected by 1.4 GHz flux density. Second, for an unbiased calculation of the 31 GHz contribution of these sources a complete 1.4 to 31 GHz (effective) spectral index distribution must be used. Populations *selected* at a higher frequency will have preferentially flatter spectral indices; and spectral indices measured between 1.4 and a higher frequency less than 31 GHz will not in general be representative, and in particular, will not reflect the steepening of synchrotron spectral indices to higher frequencies. Both of these effects, due to the large lever arm in frequency involved, have a significant impact. Third, it is essential to avoid selection biases in estimating the spectral index distribution. In the absence of better information previous CBI results used an incomplete sample of 1.4 to 31 GHz spectral indices (biased flat) resulting in an overestimate of the point source contribution. The Bayesian analysis of § 5.1 eliminates any bias due to censoring (non-detections) at 30 GHz. Fourth, as discussed in § 5.3.4, spectral index extrapolations from other frequencies are biased by source variability. Finally it is important to use an accurate form of the well-known low-frequency counts rather than simple approximations to them. All of these considerations are independent of the 31 GHz counts *per se*, which are only indirectly related to the conclusions reached: to calculate the CBI statistical correction from 31 GHz counts requires the same additional information (the distribution

of  $S_{31}/S_{1.4}$ ) as calculating the statistical correction from the 1.4 GHz counts.

We have also computed 31 GHz counts based on the low frequency counts and our distribution of spectral indices, finding  $N(> S_{31}) = 16.74 \pm 0.42 \times (S_{31}/10\text{mJy})^{-0.80 \pm 0.01} \text{ deg}^{-2}$  for  $0.5\text{ mJy} < S_{31} < 20\text{ mJy}$ , in good agreement with observed 31 GHz source counts at higher flux densities. In the mJy range these counts are 15% lower than the current counts of de Zotti et al. (2005).

The National Radio Astronomy Observatory is a facility of the National Science Foundation operated under cooperative agreement by Associated Universities, Inc. We thank the GBT and OVRO science and engineering staff for outstanding contributions to both survey projects and acknowledge support from NSF grants AST-9413935, AST-9802989, AST-0098734, and AST0206416. We thanks Gianfranco deZotti for providing us with his most recent 30 GHz source count model, and Jim Condon and Bill Cotton for useful discussions.

## REFERENCES

- Balser, D., Nikolic, B., & Prestage, R. 2006, GBT Technical Memo PTCS-PN/49.1
- Blake, C. & Wall, J. 2002, MNRAS, 337, 993
- Bondi, M., Ciliegi, P., Schinnerer, E., Smolcic, V., Jahnke, K., Carilli, C., & Zamorani, G. 2008, ArXiv e-prints, 804
- Cleary, K. A., Taylor, A. C., Waldrum, E., Battye, R. A., Dickinson, C., Davies, R. D., Davis, R. J., Genova-Santos, R., Grainge, K., Jones, M. E., Kneissl, R., Pooley, G. G., Rebolo, R., Rubiño-Martín, J. A., Saunders, R. D. E., Scott, P. F., Slosar, A., Titterton, D., & Watson, R. A. 2005, MNRAS, 360, 340
- Condon, J. 2003, GBT Technical Memo PTCS-PN/26.3
- Condon, J. J. 1992, ARA&A, 30, 575
- Condon, J. J., Cotton, W. D., Greisen, E. W., Yin, Q. F., Perley, R. A., Taylor, G. B., & Broderick, J. J. 1998, AJ, 115, 1693
- de Zotti, G., Ricci, R., Mesa, D., Silva, L., Mazzotta, P., Toffolatti, L., & González-Nuevo, J. 2005, A&A, 431, 893
- Dennett-Thorpe, J., Bridle, A. H., Laing, R. A., & Scheuer, P. A. G. 1999, MNRAS, 304, 271
- Harris, A. I., Baker, A. J., Jewell, P. R., Rauch, K. P., Zonak, S. G., O’Neil, K., Shelton, A. L., Norrod, R. D., Ray, J., & Watts, G. 2007, in Astronomical Society of the Pacific Conference Series, Vol. 375, From Z-Machines to ALMA: (Sub)Millimeter Spectroscopy of Galaxies, ed. A. J. Baker, J. Glenn, A. I. Harris, J. G. Mangum, & M. S. Yun, 82–+

- Hill, R. et al. submitted, ApJ
- Hoaglin, D., Mosteller, F., & Tukey, J. 1983, *Understanding Robust and Exploratory Data Analysis* (John Wiley and Sons)
- Hopkins, A. M., Afonso, J., Chan, B., Cram, L. E., Georgakakis, A., & Mobasher, B. 2003, AJ, 125, 465
- Hughes, P. A., Aller, H. D., & Aller, M. F. 1992, ApJ, 396, 469
- Jarosik, N., Bennett, C. L., Halpern, M., Hinshaw, G., & the Microwave Anisotropy Probe Radiometers. 2003, ApJS, 145, 413
- Jewell, P. R. & Prestage, R. M. 2004, in *Ground-based Telescopes*. Edited by Oschmann, Jacobus M., Jr. Proceedings of the SPIE, Volume 5489, pp. 312-323 (2004)., ed. J. M. Oschmann, Jr., 312–323
- Kovac, J. M., Leitch, E. M., Pryke, C., Carlstrom, J. E., Halverson, N. W., & Holzappel, W. L. 2002, Nature, 420, 772
- Laing, R. A. & Peacock, J. A. 1980, MNRAS, 190, 903
- Leitch, E. M., Readhead, A. C. S., Pearson, T. J., Myers, S. T., & Gulkis, S. 2000, ApJ, 532, 37
- Lewis, A. & Bridle, S. 2002, Phys. Rev. D, 66, 103511
- Mason, B. et al. in prep.
- Mason, B. S., Leitch, E. M., Myers, S. T., Cartwright, J. K., & Readhead, A. C. S. 1999, AJ, 118, 2908
- Mason, B. S., Pearson, T. J., Readhead, A. C. S., Shepherd, M. C., Sievers, J., Udomprasert, P. S., Cartwright, J. K., Farmer, A. J., Padin, S., Myers, S. T., Bond, J. R., Contaldi, C. R., Pen, U., Prunet, S., Pogosyan, D., Carlstrom, J. E., Kovac, J., Leitch, E. M., Pryke, C., Halverson, N. W., Holzappel, W. L., Altamirano, P., Bronfman, L., Casassus, S., May, J., & Joy, M. 2003, ApJ, 591, 540
- Myers, S. T., Contaldi, C. R., Bond, J. R., Pen, U.-L., Pogosyan, D., Prunet, S., Sievers, J. L., Mason, B. S., Pearson, T. J., Readhead, A. C. S., & Shepherd, M. C. 2003, ApJ, 591, 575
- Nikolic, B., Balser, D., & Prestage, R. 2006, GBT Technical Memo PTCS-PN/47.1
- Oh, S. P., Cooray, A., & Kamionkowski, M. 2003, MNRAS, 342, L20
- Padin, S. 2001, Caltech technical memo
- Pearson, T. J. et al. 2003, Astrophys. J., 591, 556

- Prandoni, I., Gregorini, L., Parma, P., de Ruiter, H. R., Vettolani, G., Wieringa, M. H., & Ekers, R. D. 2000, *A&AS*, 146, 31
- Prandoni, I., Parma, P., Wieringa, M. H., de Ruiter, H. R., Gregorini, L., Mignano, A., Vettolani, G., & Ekers, R. D. 2006, *A&A*, 457, 517
- Readhead, A. C. S., Lawrence, C. R., Myers, S. T., Sargent, W. L. W., Hardebeck, H. E., & Moffet, A. T. 1989, *ApJ*, 346, 566
- Readhead, A. C. S., Mason, B. S., Contaldi, C. R., Pearson, T. J., Bond, J. R., Myers, S. T., Padin, S., Sievers, J. L., Cartwright, J. K., Shepherd, M. C., Pogosyan, D., Prunet, S., Altamirano, P., Bustos, R., Bronfman, L., Casassus, S., Holzapfel, W. L., May, J., Pen, U.-L., Torres, S., & Udomprasert, P. S. 2004, *ApJ*, 609, 498
- Richards, E. A. 2000, *ApJ*, 533, 611
- Scott, D. & White, M. 1999, *A&A*, 346, 1
- Sievers, J. et al. in prep.
- Sievers, J. L., Achermann, C., Bond, J. R., Bronfman, L., Bustos, R., Contaldi, C. R., Dickinson, C., Ferreira, P. G., Jones, M. E., Lewis, A. M., Mason, B. S., May, J., Pospieszalski, M., Readhead, A. C. S., Reeves, R., Taylor, A. C., & Torres, S. 2007, *ApJ*, 660, 976
- Taylor, A. et al. in prep.
- Toffolatti, L., Argueso Gomez, F., de Zotti, G., Mazzei, P., Franceschini, A., Danese, L., & Burigana, C. 1998, *MNRAS*, 297, 117
- Waldram, E. M. 2008, private communication
- Webb, T. M., Eales, S. A., Lilly, S. J., Clements, D. L., Dunne, L., Gear, W. K., Ivison, R. J., Flores, H., & Yun, M. 2003, *ApJ*, 587, 41
- Weintraub, L. et al. in prep.
- White, R. L., Becker, R. H., Helfand, D. J., & Gregg, M. D. 1997, *ApJ*, 475, 479
- Windhorst, R. A., Miley, G. K., Owen, F. N., Kron, R. G., & Koo, D. C. 1985, *ApJ*, 289, 494
- Yun, M. S. & Carilli, C. L. 2002, *ApJ*, 568, 88